Engineering with Computers
https://doi.org/10.1007/s00366-024-02041-8

ORIGINAL ARTICLE

Phase-field modeling of fracture in viscoelastic–viscoplastic thermoset nanocomposites under cyclic and monolithic loading

Behrouz Arash[1] · Shadab Zakavati[1] · Betim Bahtiri[2] · Maximilian Jux[3] · Raimund Rolfes[2]

Received: 26 April 2024 / Accepted: 25 July 2024

Abstract
In this study, a finite deformation phase-field formulation is developed to investigate the effect of hygrothermal conditions on the viscoelastic–viscoplastic fracture behavior of epoxy nanocomposites under cyclic and monolithic loading. The formulation incorporates a definition of the Helmholtz free energy, which considers the effect of nanoparticles, moisture content, and temperature. The free energy is additively decomposed into a deviatoric equilibrium, a deviatoric non-equilibrium, and a volumetric contribution. The proposed derivation offers a realistic modeling of damage and viscoplasticity mechanisms in the nanocomposites by coupling the phase-field damage model and a viscoelastic–viscoplastic model. Numerical simulations are conducted to study the cyclic force–displacement response of both dry and saturated boehmite nanoparticle (BNP)/epoxy samples, considering BNP contents and temperature. Comparing numerical results with experimental data shows good agreement at various BNP contents. In addition, the predictive capability of the phase-field model is evaluated through simulations of notched nanocomposite plates subjected to monolithic tensile and shear loading.

Keywords Polymer nanocomposites · Viscoplasticity · Phase-field modeling · Finite deformation

1 Introduction

In the field of engineering, a major challenge is reducing the weight of structures to improve their performance and functionality for specific applications. To achieve this, researchers are focusing on both optimizing the structure and developing new materials that have superior thermo-mechanical properties but are lightweight. One such material is polymer nanocomposites, which combine the desirable attributes of polymers, such as low weight and high ductility, with the unique features of nanoparticles [1–3]. Studies have shown that boehmite nanoparticle (BNP) reinforced epoxy composites are among the most promising composites for lightweight structures due to their high strength-to-weight ratio [4]. Compared to neat epoxies, BNP/epoxy nanocomposites have significantly improved mechanical properties, including strength and fracture toughness [4–6].

To advance the material innovation, reliable models are required to predict how external conditions (such as loading rate, temperature, and moisture) and microstructural parameters (such as nanoparticle/matrix interactions) affect the material behavior of nanocomposites. Continuing research activity on polymers and their composites has led to a variety of phenomenological or physically

Shadab Zakavati, Betim Bahtiri, Maximilian Jux, Raimund Rolfes contributed equally to this work.

✉ Behrouz Arash
behrouza@oslomet.no

Shadab Zakavati
shadab.zekavati@gmail.com

Betim Bahtiri
b.bahtiri@isd.uni-hannover.de

Maximilian Jux
maximilian.jux@dlr.de

Raimund Rolfes
r.rolfes@isd.uni-hannover.de

[1] Department of Mechanical, Electrical, and Chemical Engineering, Oslo Metropolitan University, Pilestredet 35, 0166 Oslo, Norway

[2] Institute of Structural Analysis, Hannover, Germany, Leibniz Universität Hannover, Appelstraße 9A, 30167 Hannover, Niedersachsen, Germany

[3] Institute of Composite Structures and Adaptive Systems, DLR (German Aerospace Center), Lilienthalplatz 7, 38108 Brunswick, Niedersachsen, Germany

Published online: 08 August 2024

motivated constitutive models [7–12] to elucidate their nonlinear rate- and temperature-dependent behavior. Boyce et al. [13] developed a constitutive model based on a composite-type formulation considering the microstructure of semicrystalline polymers. In the model, the soft amorphous and stiff crystalline phases are treated as the matrix and fillers, respectively. Later, based on the model, Qi and Boyce [14] proposed a viscoelastic–viscoplastic constitutive model to capture the nonlinear, rate-dependent, and softening behavior of thermoplastic polyurethanes. Li et al. [15] introduced a physically-based viscoelastic constitutive model for elastomers at large deformation, where elastomers are assumed to be cross-linked networks with superimposed free chains. Nguyen et al. [11] developed and experimentally calibrated a rate-dependent damage constitutive model for epoxy resins to study the nonlinear behavior of amorphous glassy polymers. Based on the definition of Helmholtz free energy, N'Guyen et al. [16] derived a thermodynamical framework for the thermo-chemo-mechanical couplings in polymer materials at finite deformation.

However, predicting the nonlinear stress–strain response of polymer nanocomposites is more challenging due to the heterogeneous distribution of agglomerated nanoparticles in the matrix and complex interactions between the matrix and nanoparticles. To overcome these challenges, Fankhänel et al. [17] developed an atomistically-informed finite element (FE) model to investigate the material properties of BNP/epoxy nanocomposites. They used molecular simulations to characterize the interphase properties between BNPs and epoxy matrices, which were then scaled up to the continuum level. FE simulations of representative volume elements of the nanocomposites were then performed to homogenize the effective material properties. Arash et al. [6, 18] proposed a multiscale framework to calibrate a viscoelastic damage model for BNP/epoxy nanocomposites at finite deformation. The resulting model was validated through experimental–numerical testing, demonstrating its ability to accurately capture the stress–strain relationship of the nanocomposites, including nonlinear hyperelastic, rate-dependent, and softening behavior. Unger et al. [19, 20] extended the framework to characterize the thermo-viscoelastic damage behavior of BNP/epoxy nanocomposites and developed a robust parameter identification procedure.

When it comes to computational modeling of fracture in polymer nanocomposites, accurately predicting crack initiation and propagation is crucial. Research has shown that cracks are related to the generation of microvoids and microcracks in loaded polymer materials [11, 21]. As loading continues, these microvoids and microcracks will coalesce, leading to the birth of complete cracks. The damage mechanisms and nonlinear material behavior are also affected by nanoparticle contents and hygrothermal conditions [22–25].

However, FE modeling of the damage mechanisms based on the local continuum description of damage typically suffers from an inherent mesh dependence [26, 27]. This occurs when displacement discontinuities are introduced in numerical methods with a continuous displacement field. One way to address these discontinuities is to use remeshing techniques based on the linear elastic fracture mechanics or the cohesive zone model at the element boundaries [28, 29]. The discontinuities can also be addressed by employing the embedded strong discontinuity approach and the extended FE method at the intra-element level [30–32]. While the linear elastic fracture mechanics and cohesive zone model are popular due to their simplicity and effectiveness in specific applications, they require additional criteria to study crack initiation, propagation, and branching [33]. In the enriched FE methods, the discontinuities can be incorporated into the approximation space by enhancing the kinematics of FE. However, despite the advantages of these discrete fracture mechanics models, explicitly tracking the discontinuity surface in these models can be a difficult task, especially for problems with arbitrary and complex crack paths [34]. Consequently, modeling complex fracture problems remains a challenging issue.

To overcome these issues and investigate damage and failure in materials, regularized solutions have been proposed in the literature. Various models have been developed based on regularization theories, such as the gradient-enhanced damage model and its variations [35–39]. These models include the phase-field model (PFM) [40–42], which provides variational fracture models by minimizing potential energy consisting of the bulk energy, external forces work, and surface energy. PFMs use a scalar phase-field parameter to describe the smooth transition from an intact material to a fully broken state, making them an alternative to discontinuous crack modeling. They are capable of predicting complex patterns of crack initiation, propagation, and branching. PFMs have been used to study brittle, quasi-brittle, and ductile fracture [43–51]. Shanthraj et al. [52] formulated a PFM for elasto-viscoplastic materials, which gives a physically realistic description of the material behaviour at the crack tip. Dean at al. [53] developed a PFM for long fiber polymer composites by encompassing the differentiation of fiber and matrix failure phenomena. The formulation incorporates plastic effects via an invariant-based plasticity model for matrix-dominated deformation states. Msekh et al. [54] developed a PFM to predict the tensile strength and fracture toughness of clay/epoxy nanocomposites, while Goswami et al. [55, 56] proposed a neural network algorithm for phase-field modeling of fracture in brittle materials. The simulation results show that the proposed approach can match the crack paths reported in the literature.

Furthermore, some phase-field formulations have been derived to study the rate-dependent fracture of

solids [57–60]. In the case of polymer nanocomposites, Arash et al. [24, 39] developed a phase-field formulation to study the nonlinear viscoelastic fracture behavior of BNP/epoxy nanocomposites at finite deformation, considering the effect of hygrothermal conditions. The formulation takes into account the effect of temperature, moisture, and nanoparticle contents, and defines the Helmholtz free energy through an additive decomposition of energy into equilibrium, non-equilibrium, and volumetric contributions, with varying definitions under compressive and tensile loading.

In addition to the above-mentioned inelastic mechanisms (i.e., nonlinear viscoelasticity and damage), experimental observations suggest the presence of additional irreversible deformation in nanocomposites subjected to cyclic load-unloading [23]. This indicates that the nanocomposites undergo viscoplastic deformation, which could significantly affect their overall behavior. Hence, for the more realistic modeling of these materials, a phase-field formulation, which incorporates both nonlinear viscoelasticity and viscoplasticity, is necessary.

To address the issue, this study focuses on developing a PFM to investigate the cyclic viscoelastic–viscoplastic fracture behavior of BNP/epoxy nanocomposites under hygrothermal conditions. For this, a PFM with a fracture mechanics-based crack driving force is developed, considering the effect of nanoparticles, moisture content, and temperature. Meanwhile, dogebone tensile tests under dry and saturated conditions are conducted to calibrate and validate the proposed PFM at various BNP contents. The numerical–experimental comparison reveals that the PFM can accurately predict the damage and viscoplasticity mechanisms in the nanocomposites. Furthermore, the predictive capability of the model is qualitatively evaluated through simulations of notched nanocomposite plates subjected to monolithic tensile and shear loading.

This work is organized as follows. Section 2 presents a viscoelastic–viscoplastic model describing the rate- and temperature-dependent behavior of the BNP/epoxy nanocomposites at finite deformation. In Sect. 3, the governing equations of the PFM and the corresponding weak form and discretized equations are provided. In Sect. 4, numerical simulations are presented to validate the proposed PFM and study the effect of nanoparticle content, moisture and temperature on the fracture evolution in the nanocomposites. Finally, Sect. 5 summarizes the findings.

2 Constitutive model for nanoparticle/epoxy

In this section, a viscoelastic–viscoplastic model illustrated in Fig. 1 is presented for BNP/epoxy nanocomposites. The stress response comprises of an equilibrium, two viscous,

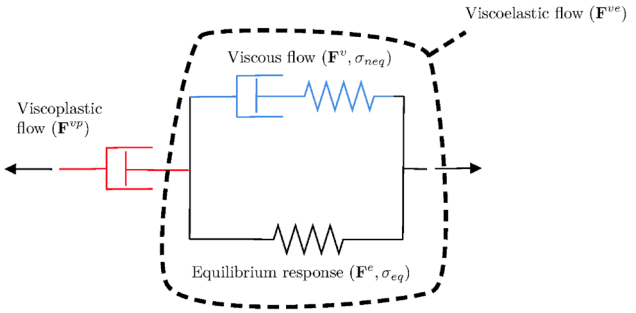

Fig. 1 One-dimensional schematic of the viscoelastic-viscoplastic constitutive model

and a volumetric component to capture the nonlinear rate-dependent behavior of materials. The effect of BNPs and moisture on the stress–strain relationship is taken into account by defining an amplification factor as a function of the nanofiller and moisture contents. A modified Kitagawa model is also adopted to account for the effect of temperature.

2.1 Kinematics

The total deformation gradient, containing the mechanical deformation, is multiplicatively split into a volumetric and deviatoric part as

$$\mathbf{F} = J^{1/3}\bar{\mathbf{F}}, \tag{1}$$

where $J = \det[\mathbf{F}]$ and $\bar{\mathbf{F}}$ are the volumetric deformation and the deviatoric deformation gradient, respectively. The volume deformation is further decomposed into two terms: the mechanical compressibility J_m, the thermal dilatation J_θ, and the moisture-induced swelling J_w, leading to an overall volumetric deformation as

$$J = J_m J_\theta J_w, \tag{2}$$

where

$$J_\theta = 1 + \alpha_\theta\left(\theta - \theta_0\right), \tag{3}$$

and

$$J_w = 1 + \alpha_w w_w. \tag{4}$$

In the equation above, α_θ and α_w are, respectively, the thermal expansion and the moisture swelling coefficient, θ is the absolute temperature, $\theta_0 = 296$ K is the reference temperature, and w_w is the moisture content [24]. Our model incorporates experimental characteristics by decomposing the material behavior into a viscoelastic and a viscoplastic part, corresponding to the time-dependent reversible and time-dependent irreversible response, respectively. We

further decompose the viscoelastic stress response into a hyperelastic network and a viscous network. The hyperelastic spring, associated with the entropy change due to deformations, captures the equilibrium response, while the viscous network composed of an elastic spring and a viscoelastic dashpot describes the non-equilibrium behavior of the nanocomposites.

The deviatoric part of the deformation gradient is decomposed into a viscoplastic and a viscoelastic component [61]:

$$\bar{\mathbf{F}} = \bar{\mathbf{F}}_{ve}\bar{\mathbf{F}}_{vp}. \tag{5}$$

Also, the viscoelastic deformation gradient is split into an elastic and an inelastic part as

$$\bar{\mathbf{F}}_{ve} = \bar{\mathbf{F}}_{e}\bar{\mathbf{F}}_{v}. \tag{6}$$

Accordingly, similar decompositions are obtained for the left Cauchy–Green deformation tensors:

$$\bar{\mathbf{B}} = \bar{\mathbf{F}}\bar{\mathbf{F}}^{T}, \tag{7}$$

$$\bar{\mathbf{B}}_{e} = \bar{\mathbf{F}}_{e}\bar{\mathbf{F}}_{e}^{T}, \tag{8}$$

$$\bar{\mathbf{B}}_{ve} = \bar{\mathbf{F}}_{ve}\bar{\mathbf{F}}_{ve}^{T}. \tag{9}$$

The total velocity gradient of the viscoelastic network, $\bar{\mathbf{L}}_{ve} = \dot{\bar{\mathbf{F}}}_{ve}\left(\bar{\mathbf{F}}_{ve}\right)^{-1}$, can be decomposed into an elastic and a viscous component analogously to Eq. (6)

$$\bar{\mathbf{L}}_{ve} = \bar{\mathbf{L}}_{e} + \bar{\mathbf{F}}_{e}\bar{\mathbf{L}}_{e}\bar{\mathbf{F}}_{e}^{-1} = \bar{\mathbf{L}}_{e} + \tilde{\mathbf{L}}_{v}, \tag{10}$$

and

$$\tilde{\mathbf{L}}_{v} = \dot{\bar{\mathbf{F}}}_{v}\bar{\mathbf{F}}_{v}^{-1} = \tilde{\mathbf{D}}_{v} + \tilde{\mathbf{W}}_{v}. \tag{11}$$

Here, a tilde ($\sim$) is used to denote the intermediate configuration. $\tilde{\mathbf{D}}_{v}$ represents the rate of the viscous deformation and $\tilde{\mathbf{W}}_{v}$ is a skew-symmetric tensor representing the rate of stretching and spin, respectively. With no loss in generality as shown in [14, 62], we make the intermediate state unique by prescribing $\tilde{\mathbf{W}}_{v} = \mathbf{0}$. The rate of the viscoelastic flow is described by

$$\tilde{\mathbf{D}}_{v} = \frac{\dot{\varepsilon}_{v}}{\tau_{neq}}\,\mathrm{dev}\left[\boldsymbol{\sigma}'_{neq}\right] \tag{12}$$

where $\tau_{neq} = \| \mathrm{dev}[\boldsymbol{\sigma}_{neq}] \|_F$ represents the Frobenius norm of the driving stress, $\dot{\varepsilon}^{v}$ is the viscous flow and $\boldsymbol{\sigma}'_{neq} = \mathbf{R}_{e}^{T}\boldsymbol{\sigma}_{neq}\mathbf{R}_{e}$ represents the stress acting on the viscous component in its relaxed configuration. The viscous flow is defined by the Argon model

$$\dot{\varepsilon}_{v} = \dot{\varepsilon}_{0}\exp\left[\frac{\Delta H}{k_{b}T}\left(\left(\frac{\tau_{neq}}{\tau_{0}}\right)^{m} - 1\right)\right], \tag{13}$$

where k_b, $\dot{\varepsilon}_0$, ΔH and τ_0 are the Boltzmann constant, a pre-exponential factor, the activation energy and the athermal yield stress. Recent models [63] have shown a better agreement with experimental data by using the exponential factor m as a material parameter and therefore reconcile the moisture- or temperature dependency of the stiffness with the softening of the viscoelastic flow. We also modify the athermal yield stress of the argon model and propose a non-linear behavior of the athermal yield stress driven by the local chain stretch Λ_{chain}, in contrast to the linear modification proposed by [14].

It can be shown that the time derivative of $\dot{\bar{\mathbf{F}}}_{v}$ can be derived from Eqs. (11) and (12) as follows [64]:

$$\dot{\bar{\mathbf{F}}}_{v} = \bar{\mathbf{F}}_{e}^{-1}\dot{\varepsilon}_{v}\frac{\mathrm{dev}\left[\boldsymbol{\sigma}'_{neq}\right]}{\tau_{neq}}\bar{\mathbf{F}}_{ve}. \tag{14}$$

Similarly, the total velocity gradient of the overall network, $\bar{\mathbf{L}} = \dot{\bar{\mathbf{F}}}(\bar{\mathbf{F}})^{-1}$, can be expanded to the following:

$$\bar{\mathbf{L}} = \bar{\mathbf{L}}_{ve} + \bar{\mathbf{L}}_{ve}\bar{\mathbf{L}}_{vp}\bar{\mathbf{F}}_{ve}^{-1} = \bar{\mathbf{L}}_{ve} + \tilde{\mathbf{L}}_{vp}. \tag{15}$$

Again, we consider the viscoplastic velocity gradient to be additively decomposed into the symmetric rate of stretching and the skew-symmetric rate of spinning:

$$\tilde{\mathbf{L}}_{vp} = \dot{\bar{\mathbf{F}}}_{vp}\bar{\mathbf{F}}_{vp}^{-1} = \tilde{\mathbf{D}}_{vp} + \tilde{\mathbf{W}}_{vp}, \tag{16}$$

and we take $\tilde{\mathbf{W}}_{vp} = \mathbf{0}$ again leading to:

$$\tilde{\mathbf{D}}_{vp} = \frac{\dot{\varepsilon}_{vp}}{\tau_{tot}}\,\mathrm{dev}[\boldsymbol{\sigma}], \tag{17}$$

where $\mathrm{dev}[\boldsymbol{\sigma}]$ is the deviatoric part of the total stress and $\tau_{tot} = \| \mathrm{dev}[\boldsymbol{\sigma}] \|_F$. To characterize the viscoplastic flow $\dot{\varepsilon}_{vp}$, we implement a simple phenomenological representation as follows:

$$\dot{\varepsilon}_{vp} = \begin{cases} 0 & \tau_{tot} < \sigma_0 \\ a(\epsilon - \epsilon_0)^{b}\dot{\epsilon} & \tau_{tot} \geq \sigma_0 \end{cases}, \tag{18}$$

where a, b and σ_0 are material parameters. ϵ_0 is the stress at which the viscoplastic flow is activated, represented by the Frobenius norm of the Green strain tensor $\| \mathbf{E} \|_F$, which is derived from the deformation gradient:

$$\mathbf{E} = \frac{1}{2}\left(\mathbf{F}^{T}\mathbf{F} - \mathbf{I}\right), \tag{19}$$

and $\dot{\epsilon}$ is the strain rate of the effective strain $\| \mathbf{E} \|_F$, thus introducing a simple strain-rate dependency of the

viscoplastic flow. Analogous to Eq. (14), the time derivative of the viscoplastic deformation gradient is given by

$$\dot{\bar{\mathbf{F}}}_{vp} = \bar{\mathbf{F}}_{ve}^{-1}\dot{\varepsilon}_{vp}\frac{\mathrm{dev}\left[\boldsymbol{\sigma}_{tot}\right]}{\tau_{tot}}\bar{\mathbf{F}}, \tag{20}$$

characterizing the rate kinematics of the viscoplastic flow. We obtain the viscous and viscoplastic deformation gradients at the end of a time increment using the Euler backward time integration.

In Eqs. (20) and (14), the midpoint method is used to numerically obtain the inelastic deformation gradient at the end of a time increment, i.e.,

$$\bar{\boldsymbol{F}}_{v/vp}^{t+\frac{dt}{2}} = \bar{\boldsymbol{F}}_{v/vp}^{t} + \frac{dt}{2}\dot{\bar{\boldsymbol{F}}}_{v/vp}^{t}, \tag{21}$$

$$\bar{\boldsymbol{F}}_{v/vp}^{t+dt} = \bar{\boldsymbol{F}}_{v/vp}^{t} + dt\dot{\bar{\boldsymbol{F}}}_{v/vp}^{t+\frac{dt}{2}}. \tag{22}$$

To calculate the elastic deformation gradient at the midpoint, it is also required to find the total deformation gradient at the midpoint. This is done by taking the average of the deformation gradient at the start and end of the increment

$$\bar{\boldsymbol{F}}^{t+\frac{dt}{2}} = \frac{\bar{\boldsymbol{F}}^{t} + \bar{\boldsymbol{F}}^{t+dt}}{2}. \tag{23}$$

The equations to be solved for each time increment are summarized in Table 1.

2.2 Phenomenological viscoelastic–viscoplastic model coupled with a phase-field description

Following the additive decomposition of the free energy proposed in [46], the overall free energy of the material can be decomposed into an equilibrium ψ_{eq}, a non-equilibrium ψ_{neq} and a volumetric part ψ_{vol} as

$$\psi\left(\bar{\boldsymbol{B}}_{ve}, \bar{\boldsymbol{B}}_{e}, J, \phi\right) = g(\phi)\left(\psi_{eq}\left(\bar{\boldsymbol{B}}_{ve}\right) + \psi_{neq}\left(\bar{\boldsymbol{B}}_{e}\right) + \psi_{vol}(J)\right), \tag{24}$$

The energetic degradation function $g(\phi)$ captures the evolution of the strain energy versus the phase-field variable ($\phi \in [0,1]$) and satisfies the following conditions

$$g(0) = 1,\ g(1) = 0,\ g'(\phi) \leq 0 \text{ and } g'(1) = 0. \tag{25}$$

The conditions prescribe a monotonic decreasing behavior during the fracture evolution.

Here, the equilibrium ψ_{eq} and non-equilibrium ψ_{neq} parts of the free energy are defined by the neo-Hookean hyperelastic model as

$$\rho_0\psi_{eq} = \frac{1}{2}\mu_{eq}\left(v_{np}, \theta, w_w\right)\left(I_1\left(\bar{\boldsymbol{B}}_{ve}\right) - 3\right), \tag{26}$$

and

$$\rho_0\psi_{neq} = \frac{1}{2}\mu_{neq}\left(v_{np}, \theta, w_w\right)\left(I_1\left(\bar{\boldsymbol{B}}_{e}\right) - 3\right), \tag{27}$$

where $I_1(\cdot) = \mathrm{tr}[\cdot]$ is the first invariant of the tensor, μ_{eq} and μ_{neq} are BNP content-, temperature- and moisture content-dependent material parameters, and ρ_0 is the initial density. The material parameters μ_{eq} and μ_{neq} depend on temperature, BNP volume fraction v_{np} and water content w_w

$$\mu_{eq}\left(v_{np}, \theta, w_w\right) = X\left(v_{np}, w_w\right)\mu_{eq}^{0}(\theta), \tag{28}$$

$$\mu_{neq}\left(v_{np}, \theta, w_w\right) = X\left(v_{np}, w_w\right)\mu_{neq}^{0}(\theta). \tag{29}$$

Assuming that BNPs are well-dispersed rigid particles in the epoxy matrix, the Guth–Gold model is adopted by which the effective stiffness of particle-filled solids is obtained by $\langle E\rangle = XE_m$, where E_m is the stiffness of matrix [65]. The amplification factor X is typically a function of fillers' volume fraction and distribution. So far, some attempts of various levels of sophistication have been conducted to incorporate the effect of particle/matrix interactions on the effective modulus of polymer composites. Most of these models suggest a polynomial series expansion for the amplification factor. Here, a modified Guth–Gold model suggested in [24] is used to account for uniformly distributed nanoparticles and moisture content as follows

$$X = \left(1 - 9.5w_w + 0.057w_w^2\right)\left(1 + 3.5v_{np} + 18v_{np}^2\right). \tag{30}$$

In Eq. (30), the effect of moisture content on the material behavior is taken into account based on experimental data. The modified amplification factor proposed in this work is a first step to capture the stress–strain behavior of BNP/epoxy nanocomposites under hygrothermal conditions. Furthermore, to consider the effect of temperature on the material

Table 1 Summary of step-by-step algorithm for each time increment

1. Known values at time t: Deformation gradient ($\boldsymbol{F}$), and state variables ($\bar{\mathbf{F}}_{v}$, $\bar{\mathbf{F}}_{vp}$)
2. Known values at time $t + dt$: Deformation gradient $\boldsymbol{F}$
3. Calculate $\bar{\mathbf{F}}_{v}$ at $t + dt$ using Eq. (14) and the time integration equations presented in Eqs. ()–()
4. Calculate $\bar{\mathbf{F}}_{vp}$ at $t + dt$ using Eq. (20) and the time integration equations presented in Eqs. ()–()

properties, a modified Kitagawa model proposed by Unger et al. [20] is utilized with the following equations:

$$\mu_{eq}^{0} = \mu_{eq,ref}^{0}\left(2 - \exp\left[\alpha\left(\theta - \theta_0\right)\right]\right), \tag{31}$$

$$\mu_{neq}^{0} = \mu_{neq,ref}^{0}\left(2 - \exp\left[\alpha\left(\theta - \theta_0\right)\right]\right). \tag{32}$$

The volumetric part of the free energy ψ_{vol} is also defined by

$$\rho_0\psi_{vol} = \frac{1}{2}k_v\left(\frac{J_m^2 - 1}{2} - \ln\left[J_m\right]\right)^2, \tag{33}$$

where the bulk modulus is assumed to be $k_v = \left(2 - \exp\left[\alpha\left(\Theta - \theta_0\right)\right]\right)Xk_v^0$, and k_v^0 is the bulk modulus at room temperature. The total stresses are then obtained from

$$\boldsymbol{\sigma} = g\left(\boldsymbol{\sigma}_{dev} + \boldsymbol{\sigma}_{vol}\right) \tag{34}$$

where

$$\boldsymbol{\sigma}_{dev} = J^{-1}\left(\mu_{eq}\bar{\boldsymbol{B}}_{ve}^{D} + \mu_{neq}\bar{\boldsymbol{B}}_{e}^{D}\right), \tag{35}$$

and

$$\boldsymbol{\sigma}_{vol} = \frac{1}{2}k_v J_\theta^{-1}\left(J_m - \frac{1}{J_m}\right)\mathbf{1}. \tag{36}$$

Here, $\mathbf{1}$ is the identity tensor. The constitutive model is able to capture the nonlinear elasticitiy at finite deformation, the nonlinear viscoelastic behavior, viscoplastic flow because of stress driven chain sliding, and the effect of temperature and moisture content on the stress–strain relationship.

3 Phase-field model at finite deformation

To evaluate the predictive capability of the proposed constitutive model, we use the model to present a formulation of the PFM for nanoparticle/polymer composites. This section presents a variational phase-field formulation for quasi-brittle fracture at finite deformation, the continuum mechanics incremental scheme and FE equations are derived to show the procedure of analysis.

3.1 Problem field description

The strong form of the boundary value problem in the referential configuration for the coupled displacement $\boldsymbol{u}$ and phase-field variable ϕ can be written as

$$\boldsymbol{\nabla}_{\boldsymbol{X}}.\boldsymbol{P} + \boldsymbol{B} = \mathbf{0} \text{ in } \Omega_0 \tag{37}$$

$$\boldsymbol{P}.\mathbf{N} = \bar{\boldsymbol{T}} \text{ on } \Gamma_0 \tag{38}$$

$$\frac{G_c}{l_0}\phi - G_c l_0 \boldsymbol{\nabla}_{\boldsymbol{X}}.\left(\boldsymbol{\nabla}_{\boldsymbol{X}}\phi.\mathbf{C}^{-1}\right) = -g'(\phi)\mathcal{H} \text{ in } \Omega_0 \tag{39}$$

$$\boldsymbol{\nabla}_{\boldsymbol{X}}\phi.\boldsymbol{N} = 0 \text{ in } \Gamma_0, \tag{40}$$

from which the Euler–Lagrange equations in the spatial form are obtained as

$$\boldsymbol{\nabla}_{\boldsymbol{x}}.\boldsymbol{\sigma} + \boldsymbol{b} = \mathbf{0} \text{ in } \Omega_t \tag{41}$$

$$\boldsymbol{\sigma}.\mathbf{n} = \bar{\boldsymbol{t}} \text{ on } \Gamma_t \tag{42}$$

$$\frac{G_c}{l_0}\phi - G_c l_0 \boldsymbol{\nabla}_{\boldsymbol{x}}.\boldsymbol{\nabla}_{\boldsymbol{x}}\phi = -g'(\phi)\mathcal{H} \text{ in } \Omega_t \tag{43}$$

$$\boldsymbol{\nabla}_{\boldsymbol{x}}\phi.\boldsymbol{n} = 0 \text{ in } \Gamma_t, \tag{44}$$

where $\boldsymbol{P}$ and $\boldsymbol{\sigma}$ are the first Piola–Kirchhoff stress and the Cauchy stress, respectively, and $\boldsymbol{C} = \boldsymbol{F}^T\boldsymbol{F}$ is the right Cauchy–Green deformation tensor. The coupled equations in the the spatial configuration is formulated by $\boldsymbol{\sigma} = \boldsymbol{P}\text{cof}\left(\mathbf{F}^{-1}\right)$, $\boldsymbol{\nabla}_X(\cdot) = \boldsymbol{\nabla}_x(\cdot)\mathbf{F}$ and $\boldsymbol{b} = J^{-1}\boldsymbol{B}$, where $\text{cof}(\mathbf{F}) = J\mathbf{F}^{-T}$.

In the equations above, l_0 is the length scale that controls the width of the diffuse crack. It is a numerical parameter used to regularize sharp cracks, and it is also considered a material parameter that is experimentally calibrated [66]. $\Gamma = \Gamma_t \cup \Gamma_u$, $\boldsymbol{B}$ and $\boldsymbol{b}$ respetively represent the vector of body forces in the referential and spatial configuration, $\boldsymbol{N}$ and $\boldsymbol{n}$ are respectively the outward unit normal vector on the boundary Γ_0 of the body Ω_0 and the boundary Γ_t of the body Ω_t, and $\boldsymbol{T}$ and $\boldsymbol{t}$ are respectively the traction force in the referential and spatial configuration.

To take into account the effect of BNP content on the fracture evolution in the nanocomposites, the energy release rate is taken to be $G_c = XG_c^0$. To account for the tension-compression asymmetry, the variational formulation has to be modified. However, there is no general method to split the energy into tensile and compressive components. All decompositions are somewhat arbitrarily and at best justified by mathematical considerations. Here, to realisticly model damage and viscoplasticity mechanisms in the nanocomposites, a fracture mechanical-based crack-driving force proposed in [67] is chosen as follows

$$\mathcal{H}(t) = \max_{\tau\in[0,t]}\mathcal{Y}, \tag{45}$$

where

$$\mathcal{Y} = \frac{G_c}{l_0}\langle\sigma_m\rangle_+\left\langle\frac{\sigma_I}{\sigma_d} - 1\right\rangle_+, \tag{46}$$

and σ_m is the mean stress defined by

$$\sigma_m = \left(\sigma_I + \sigma_{II} + \sigma_{III}\right)/3. \tag{47}$$

Here, $\langle a \rangle_+ := \frac{1}{2}(a + |a|)$, σ_d is a material parameter, and $\sigma_I \geq \sigma_{II} \geq \sigma_{III}$ are the principal stresses (i.e., the eigenvalues of the Cauchy stress tensor). Notably, while variationally determined crack-driving forces are applicable to simple-structured materials, extending them to materials with complex microstructures and highly nonlinear, rate- and temperature-dependent behavior under complex loading conditions is unfeasible. Therefore, we use a physically motivated crack-driving force postulated from a failure criterion. This allows modeling fracture in the epoxy nanocomposites consistent with experimental observations.

$\mathcal{H}$ ensures the positive evolution of the phase field variable, which prevents the healing of cracks. Also, a monotonically decreasing degradation function $g(\phi)$, satisfying conditions presented in Eq. (48), is given by

$$g(\phi) = (1-\phi)^2 + k, \tag{48}$$

where k is a small positive parameter introduced for ensuring the stability of the solution [42].

To obtain the weak form of the governing equations, the weighted residual approach is used. Accordingly, Eqs. (37) and (39) multiplied by weight functions and integrated over Ω_0. Using the divergence theorem and imposing the boundary conditions, the weak form of the governing equations is obtained as follows

$$\begin{aligned} &\int_{\Omega_0} \boldsymbol{P} : \boldsymbol{\nabla}_X \boldsymbol{\eta}_u \mathrm{d}V - \int_{\Omega_0} \rho_0 \boldsymbol{B} \cdot \boldsymbol{\eta}_u \mathrm{d}V \\ &- \int_{\Gamma_0} \bar{\boldsymbol{T}} \cdot \boldsymbol{\eta}_u \mathrm{d}A = 0 \quad \forall\, \boldsymbol{\eta}_u \in H_0^1(\Omega), \end{aligned} \tag{49}$$

and

$$\begin{aligned} &\int_{\Omega_0} \left(g'(\phi)\mathcal{H}\eta_\phi + \frac{G_c}{l_0}\phi\eta_\phi - G_c l_0 \boldsymbol{\nabla}_X \phi \cdot \mathbf{C}^{-1} \cdot \boldsymbol{\nabla}_X \eta_\phi \right) \mathrm{d}V \\ &= 0 \quad \forall \quad \eta_\phi \in H_0^1(\Omega). \end{aligned} \tag{50}$$

The weak form in the spatial description can then be derived as

$$\begin{aligned} &\int_{\Omega_t} \boldsymbol{\sigma} : \boldsymbol{\nabla}_x \boldsymbol{\eta}_u \mathrm{d}v - \int_{\Omega_t} \rho_t \boldsymbol{b} \cdot \boldsymbol{\eta}_u \mathrm{d}v - \int_{\Gamma_t} \bar{\boldsymbol{t}} \cdot \boldsymbol{\eta}_u \mathrm{d}a \\ &= 0 \quad \forall\, \boldsymbol{\eta}_u \in H_0^1(\Omega), \end{aligned} \tag{51}$$

and

$$\begin{aligned} &\int_{\Omega_t} \left(J^{-1} g'(\phi)\mathcal{H}\eta_\phi + J^{-1}\frac{G_c}{l_0}\phi\eta_\phi - J^{-1} G_c l_0 \boldsymbol{\nabla}_x \phi \cdot \boldsymbol{\nabla}_x \eta_\phi \right) \mathrm{d}v \\ &= 0 \quad \forall\, \eta_\phi \in H_0^1(\Omega). \end{aligned} \tag{52}$$

The Eqs. (51) and (52) in terms of spatial arguments are formulated using $dv = JdV$ and $\boldsymbol{n}da = cof(\mathbf{F})$.

3.2 Consistent incremental-iterative scheme

Assuming that only deformation-independent loads act on the body, Eqs. (49) and (50) can then be expressed in terms of external and internal nodal forces as

$$r^u = f^u_{int} - f^u_{ext} = 0, \tag{53}$$

$$r^\phi = f^\phi_{int} - f^\phi_{ext} = 0, \tag{54}$$

where

$$f^u_{int} = \int_{\Omega_0} \boldsymbol{P} : \boldsymbol{\nabla}_X \boldsymbol{\eta}_u \mathrm{d}V, \tag{55}$$

$$f^u_{ext} = \int_{\Omega_0} \rho_0 \boldsymbol{B} \cdot \boldsymbol{\eta}_u \mathrm{d}V - \int_{\Omega_0} \bar{\boldsymbol{T}} \cdot \boldsymbol{\eta}_u \mathrm{d}A, \tag{56}$$

$$\begin{aligned} f^\phi_{int} = \int_{\Omega_t} \Big(&J^{-1} g'(\phi)\mathcal{H}\eta_\phi + J^{-1}\frac{G_c}{l_0}\phi\eta_\phi \\ &- J^{-1} G_c l_0 \boldsymbol{\nabla}_x \phi \cdot \boldsymbol{\nabla}_x \eta_\phi \Big) \mathrm{d}v, \end{aligned} \tag{57}$$

$$f^\phi_{ext} = 0, \tag{58}$$

By linearizing Eqs. (53) and (54) at iteration $i+1$ with respect to the previous iteration i, a consistent tangent stiffness is obtained as follows

$$r^u_{i+1} = r^u_i + \triangle r^u = 0, \tag{59}$$

$$r^\phi_{i+1} = r^\phi_i + \triangle r^\phi, \tag{60}$$

where

$$\triangle r^u = D_u r^u_i \cdot \triangle \mathbf{u} + D_\phi \mathbf{r}^u_i \cdot \triangle \phi \tag{61}$$

and

$$\triangle r^\phi = D_u r^\phi_i \cdot \triangle \mathbf{u} + D_\phi r^\phi_i \cdot \triangle \phi. \tag{62}$$

The linearization of Eqs. (51) and (52) in spatial formulation can finally be obtained using a push fowrard of the linearized equation in the referential configuration

$$\begin{aligned}&\int_{\Omega_t}\left(\boldsymbol{\nabla}_{\boldsymbol{x}}\triangle\mathbf{u}\cdot\boldsymbol{\sigma}\cdot\boldsymbol{\nabla}_{\boldsymbol{x}}\boldsymbol{\eta}_u+\boldsymbol{\nabla}^s_{\boldsymbol{x}}\boldsymbol{\eta}_u\cdot\hat{\boldsymbol{c}}\cdot\boldsymbol{\nabla}^s_{\boldsymbol{x}}\triangle\mathbf{u}\right)\mathrm{d}v\\&+\int_{\Omega_t}\left(\boldsymbol{\nabla}^s_{\boldsymbol{x}}\boldsymbol{\eta}_u\cdot D_\phi\boldsymbol{\sigma}\cdot\triangle\phi\right)\mathrm{d}v\\&=f^u_{ext}-f^u_{int,i}\end{aligned}\tag{63}$$

and

$$\begin{aligned}&\int_{\Omega_t}\left(J^{-1}g'(\phi)2\frac{\partial\mathcal{H}}{\partial\mathbf{g}}\cdot\boldsymbol{\nabla}_x\triangle\mathbf{u}\eta_\phi\right)\mathrm{d}v\\&+\int_{\Omega_t}\left(J^{-1}g''(\phi)\mathcal{H}\triangle\phi\eta_\phi+J^{-1}\frac{G_c}{l_0}\triangle\phi\eta_\phi+J^{-1}G_cl_0\boldsymbol{\nabla}_{\boldsymbol{x}}\triangle\phi\cdot\nabla_x\eta_\phi\right)\mathrm{d}v\\&=f^\phi_{ext}-f^\phi_{int,i}\end{aligned}\tag{64}$$

In the equations above, $\hat{\boldsymbol{c}}=J^{-1}\mathbf{c}=\frac{\partial\boldsymbol{S}}{\partial\boldsymbol{C}}$ is the tangent moduli, and $\boldsymbol{S}$ is the second Piola–Kirchhoff stress. Also, $\frac{\partial(\cdot)}{\partial\boldsymbol{g}}=\boldsymbol{F}\frac{\partial(\cdot)}{\partial\boldsymbol{C}}\boldsymbol{F}^T$.

3.3 Finite element formulation

The linearized equilibrium and phase-field equations are finally summarized in the following system of equations:

$$\begin{bmatrix}\mathbf{K}^{uu}_i&\mathbf{K}^{u\phi}_i\\\mathbf{K}^{\phi u}_i&\mathbf{K}^{\phi\phi}_i\end{bmatrix}\begin{bmatrix}\triangle\mathbf{u}_{i+1}\\\triangle\boldsymbol{\phi}_{i+1}\end{bmatrix}=\begin{bmatrix}\mathbf{f}^u_{ext}\\\mathbf{f}^\phi_{ext}\end{bmatrix}-\begin{bmatrix}\mathbf{f}^u_{int,i}\\\mathbf{f}^\phi_{int,i}\end{bmatrix}\tag{65}$$

where

$$\mathbf{K}^{uu}_i=\int_\Omega\mathbf{B}^T_u\hat{\boldsymbol{c}}\mathbf{B}_u\mathrm{d}\Omega+\int_\Omega\mathbf{B}^T_u\boldsymbol{\sigma}\mathbf{B}_u\mathrm{d}\Omega,\tag{66}$$

$$\mathbf{K}^{u\phi}_i=\int_\Omega\mathbf{B}^T_u\left(\frac{\partial\boldsymbol{\sigma}}{\partial\phi}\right)\mathbf{N}_\phi\mathrm{d}\Omega,\tag{67}$$

$$\mathbf{K}^{\phi u}_i=\int_\Omega\mathbf{N}^T_\phi\left(J^{-1}g'\frac{2\partial\mathcal{H}}{\partial\boldsymbol{g}}\right)\mathbf{B}_u\mathrm{d}\Omega,\tag{68}$$

$$\mathbf{K}^{\phi\phi}_i=\int_\Omega J^{-1}\left(\mathbf{N}^T_\phi\left(g''\mathcal{H}+\frac{G_c}{l_0}\right)\mathbf{N}_\phi+G_cl_0\mathbf{B}^T_\phi\mathbf{B}_\phi\right)\mathrm{d}\Omega,\tag{69}$$

In the equations above, the shape function matrices $\boldsymbol{N}_u$ and $\boldsymbol{N}_\phi$ interpolate the nodal values $\boldsymbol{u}$ and $\boldsymbol{\phi}$, respectively, and $\boldsymbol{B}_u$ and $\boldsymbol{B}_\phi$ are the gradient operators for the displacement and the nonlocal equivalent strain, respectively. The same shape functions interpolate the nodal values of the weight functions $\boldsymbol{\eta}_u$ and η_ϕ.

In what follows, the two fields of the phase-field fracture problem are solved using a staggered algorithm proposed by Miehe et al. [43]. The staggered solution, which decouples the equilibrium and phase-field equations, has shown to be computationally efficient and robust through its broad application in the literature [68, 69]. Accordingly, the coupling terms $\mathbf{K}^{u\phi}_i$ and $\mathbf{K}^{\phi u}_i$ are not taken into account.

3.4 Consistent tangent moduli based on the Jaumann–Zaremba stress rate

When dealing with large rotations, it is incorrect to use just the material derivatives of the stress tensors (such as the rate of Cauchy stress), as they do not transform properly as a tensor under a superposed rigid body motion. To ensure the objectivity of the stress rate, the formulations presented in this section is used to compute the tangent that is consistent with Jaumann–Zaremba rate formulation.

In order to integrate the viscoelastic model into the incremental-iterative FE framework, the tangent modulus tensor $\mathbb{C}^{\sigma J}=\frac{\partial\boldsymbol{\sigma}}{\partial\boldsymbol{\epsilon}}$ needs to be explicitly specified. However, a closed-form calculation of the tangent tensor is not a straightforward task. Here, we use an efficient numerical approximation of the tangent moduli proposed by Sun et al. [70]. In this approach, by perturbing the deformation gradient, the tangent moduli for the Jaumann rate of the Cauchy stress are accurately approximated by a forward difference of the Cauchy stresses. The Jaumann rate of the Cauchy stress can be expressed as

$$\overset{\nabla}{\boldsymbol{\sigma}}=\dot{\boldsymbol{\sigma}}-\boldsymbol{W}\boldsymbol{\sigma}-\boldsymbol{\sigma}\boldsymbol{W}^T=\mathbb{C}^{\sigma J}:\boldsymbol{D}\tag{70}$$

The linearized incremental form of Eq. (70) is then obtained from

$$\Delta\boldsymbol{\sigma}-\Delta\boldsymbol{W}\boldsymbol{\sigma}-\boldsymbol{\sigma}\Delta\boldsymbol{W}^T=\mathbb{C}^{\sigma J}:\Delta\boldsymbol{D}\tag{71}$$

To numerically calculate components of $\mathbb{C}^{\sigma J}$, Eq. (71) is perturbed by applying small perturbations to components of $\Delta\boldsymbol{D}$ and $\Delta\boldsymbol{W}$ tensors. Here, $\Delta\boldsymbol{W}_{ij}$ and $\Delta\boldsymbol{D}_{ij}$ tensors with perturbed (i,j) components are expressed as

$$\Delta\boldsymbol{W}_{ij}=\frac{1}{2}\left(\Delta\boldsymbol{F}_{ij}\boldsymbol{F}^{-1}-\left(\Delta\boldsymbol{F}_{ij}\boldsymbol{F}^{-1}\right)^T\right),\tag{72}$$

and

$$\Delta\boldsymbol{D}_{ij}=\frac{1}{2}\left(\Delta\boldsymbol{F}_{ij}\boldsymbol{F}^{-1}+\left(\Delta\boldsymbol{F}_{ij}\boldsymbol{F}^{-1}\right)^T\right),\tag{73}$$

where the corresponding perturbed $\Delta\boldsymbol{F}_{ij}$ is obtained from perturbing its (i,j) component as [71]

$$\Delta \boldsymbol{F}_{ij} = \frac{\epsilon}{2}\left(e_i \otimes e_j \boldsymbol{F} + e_j \otimes e_i \boldsymbol{F}\right). \tag{74}$$

Here, ϵ is a perturbation parameter. According to the report in [72], using $\epsilon = 10^{-3}$ can produce good results, but smaller values can lead to even better results. Also, values smaller than 10^{-5} do not provide any additional benefit regarding the number of iterations required. By substituting Eq. (74) into Eqs. (72) and (73), we have

$$\Delta \boldsymbol{W}_{ij} = \boldsymbol{0}, \tag{75}$$

$$\Delta \boldsymbol{D}_{ij} = \frac{\epsilon}{2}\left(e_i \otimes e_j + e_j \otimes e_i\right). \tag{76}$$

It is noteworthy that $\Delta \boldsymbol{D}$ has six independent components due to its symmetry. Therefore, the choice of (i,j) would be (1,1), (2,2), (3,3), (1,2), (1,3), and (2,3). The perturbed deformation gradient $\hat{\boldsymbol{F}}_{ij}$ can then be written as

$$\hat{\boldsymbol{F}}_{ij} = \boldsymbol{F} + \Delta \boldsymbol{F}_{ij} \tag{77}$$

Using Eq. (77), $\Delta \boldsymbol{\sigma}$ is approximated by the forward difference of the perturbed and unperturbed Cauchy stresses

$$\Delta \boldsymbol{\sigma} \approx \boldsymbol{\sigma}\left(\hat{\boldsymbol{F}}_{ij}\right) - \boldsymbol{\sigma}(\boldsymbol{F}). \tag{78}$$

Substituting Eqs. (75), (76) and (78) into Eq. (71) gives

$$\boldsymbol{\sigma}\left(\hat{\boldsymbol{F}}_{ij}\right) - \boldsymbol{\sigma}(\boldsymbol{F}) \approx \mathbb{C}^{\sigma J}_{ij} : \frac{\epsilon}{2}\left(e_i \otimes e_j + e_j \otimes e_i\right). \tag{79}$$

Using Eq. (79), the numerical approximation of the tangent moduli is finally obtained as

$$\mathbb{C}^{\sigma J}_{ij} = \frac{1}{\epsilon}\left[\boldsymbol{\sigma}\left(\hat{\boldsymbol{F}}_{ij}\right) - \boldsymbol{\sigma}(\boldsymbol{F})\right] \tag{80}$$

where $\mathbb{C}^{\sigma J}_{ij}$ represents the components of the tangent modulus tensor $\mathbb{C}^{\sigma J}$ calculated by the perturbation of $\Delta \boldsymbol{F}_{ij}$. The tangent contribution, accounting for the Jaumann rate formulation, is then used in the FE analysis. Table 2 summarizes a step-by-step algorithm adopted from [73] to compute the mechanical tangent required for the FE analysis.

4 Fracture experiments and numerical simulations

This section aims to identify and validate the proposed PFM's parameters. Firstly, we compare the numerical results of dogbone tests of BNP/epoxy samples with experimental data. Then, we study the influence of temperature on the fracture evolution. Lastly, we qualitatively evaluate the model's ability to predict fracture patterns using the well-known single-edge notched tests.

4.1 Experiments

The samples used for conditioning and mechanical tests are obtained from the panels shown in Fig. 2. In epoxy systems, necking in the tension direction is not a material property

Table 2 Summary of step-by-step algorithm used to compute the tangent moduli

1. Define a perturbation parameter: $\epsilon = 10^{-5}$
2. Compute the right Cauchy-Green tensor: $\mathbf{C} = \mathbf{F}^T\mathbf{F}$
3. Calculate the Cauchy stress tensor (i.e., $\boldsymbol{\sigma}$) using equations presented in Sect. 2
4. **for** $k = 1 \ldots 3$ **do**
5. **for** $l = 1 \ldots 3$ **do**
6. Initialize $\hat{\boldsymbol{F}} = \boldsymbol{F}$
7. Perturb $\hat{\boldsymbol{F}}_{kl} = \hat{\boldsymbol{F}}_{kl} + \epsilon/2$
8. Perturb $\hat{\boldsymbol{F}}_{lk} = \hat{\boldsymbol{F}}_{lk} + \epsilon/2$
9. Calculate the corresponding perturbed stress response $\Delta\boldsymbol{\sigma}$ using Eq. (78)
10. **for** $i = 1 \ldots 3$ **do**
11. **for** $j = 1 \ldots 3$ **do**
12. Compute and store $\mathbb{C}^{\sigma J}_{ijkl}$ and $\mathbb{C}^{\sigma J}_{ijlk}$ based on the Jaumann stress rate of the Cauchy stress as presented in Eq. (80)
13. end
14. end
15. end
16. end
17. Determine the material tangent: $\mathbb{C}^{\sigma J}$
18. Store the tangent tensor in Voigt-type matrix
19. Solve the system of equations presented in Eq. (65) using a staggered algorithm [43]

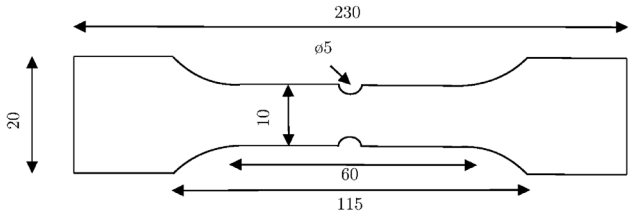

Fig. 2 Planar dimensions of the specimen for conditioning and mechanical loading-unloading tests with a thickness of 2.3 mm. All dimensions are in millimeters

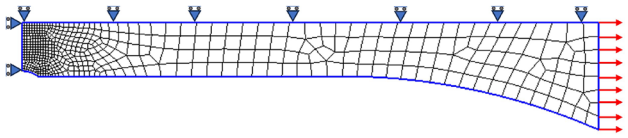

Fig. 3 Loading and boundary conditions imposed on quarter of the specimen because of symmetry, and a two-dimensional FE model composed of 1563 Q4 elements

but rather a structural instability [63]. Therefore, a notch is introduced to mitigate the effects of material imperfections and necking on the yield. The samples are conditioned at 60 °C and 85% relative humidity until they reach the saturated state at a moisture concentration of 1.0% for the neat epoxy system and 1.2% for the BNPs reinforced epoxy. The total conditioning time was 115 days. Finally, the samples are subjected to mechanical loading–unloading tests according to the DIN EN ISO 527-2 testing standard. An extensometer is used to measure the specimen's elongation, and a load rate of 1 mm/min is applied. Before the final loading cycle that led to failure, six cycles were performed by loading the specimen to a specific amplitude and unloading it until the loading force reached zero.

4.2 Simulations

The specimen's symmetry allows for a more efficient FE analysis. By using the symmetries and analyzing a quarter of the specimen, we can obtain a complete solution of the entire model with less computational cost. As illustrated in Fig. 3, the model considers the double symmetry of the sample at the mid-length and width. The uppermost side's vertical displacement and the left side's horizontal displacement of the specimen are restrained, while a horizontal displacement is applied to the right side of the specimen, as shown in the figure.

Figure 3 shows the corresponding mesh with 1563 four-noded quadrilateral (Q4) elements. Due to high-stress concentrations in the right part of the model, the mesh size is refined to around 0.1 mm in the area, while the length scale parameter is set to 0.5 mm. The load is applied via an imposed displacement at a constant deformation rate of $\dot{u} = 1$ mm/min and $\theta = 296$ K. The following simulations are performed under plane strain conditions, with the load applied through constant displacement increments of $\Delta u = 1 \times 10^{-4}$ mm. The simulations have been performed using an in-house parallel MATLAB code.

Table 3 provides the identified parameters of the PFM. The table shows that the material parameters linked with equilibrium, non-equilibrium, and viscoelastic responses, the modified Kitagawa model, moisture swelling, the energy release rate of the neat epoxy, and the length scale have been obtained from the authors' previous studies [23, 24]. Additionally, the remaining material parameters have been calibrated to achieve the best fit to the experimental data. The parameters are validated using experimental data for the epoxy system with 0 and 5% wt BNPs at dry and saturated conditions. The mass density of the neat epoxy and BNP are 1.2 and 3.0 g/cc, respectively. Accordingly, the corresponding volume fraction can be calculated to be $v_{np} = 0.0215$.

The resulting cyclic loading–unloading force–displacement curves of the dogbone tests for dry and saturated epoxy samples are compared with experimental data in Fig. 4. The experimental-numerical comparison demonstrates a good agreement between the experimental data and the numerical predictions along the whole evolution of displacement. It evidences the capability of the proposed PFM in predicting the evolution of damage and viscoplasticy mechanisms in the epoxy polymer under cyclic loading. Comparing the experimental data in Fig. 4a, b show that the ductility of the epoxy increases at the presence of moisture content. Contour plots of damage for the dry epoxy specimen at imposed displacements of 3.29, 3.34, 3.35, and 3.3504 mm are illustrated in Fig. 5, showing the evolution of the phase-field variable, ϕ, at different load steps of the simulations. These snapshots correspond to the points indicated in Fig. 4a.

The effect of the length scale parameter l_0 on the sample's response was assessed using four values: $l_0 = \{0.25, 0.5, 2, 4\}$ mm. Figure 6 illustrates that the numerical results are influenced by the length scale, consistent with previous findings in the literature [66]. As a result, the parameter is considered a material parameter and calibrated by comparing force–displacement responses in numerical and experimental tests. This comparison identifies the optimized value of $l_0 = 0.5$ mm used in the following simulations.

The results presented in Fig. 7a, b demonstrate a satisfactory agreement between the numerical predictions and experimental data for the epoxy system with 5% weight percent of BNPs in both dry and saturated conditions. Although the proposed PFM model can reasonably predict the highly nonlinear viscoelastic–viscoplastic behavior of the material,

Table 3 Materials parameters of the PFM model

	Parameter	Value	Equation	References
Equilibrium shear modulus	μ_{eq}^{0}(MPa)	760	35	[23]
Non-equilibrium shear modulus	μ_{neq}^{0}(MPa)	790	35	[23]
Volumetric bulk modulus	κ_v(MPa)	1154	36	[23]
Viscoelastic dashpot	$\dot{\varepsilon}_0\left(s^{-1}\right)$	1.0447 x 10^{12}	13	[23]
	$\Delta H(J)$	1.977 x 10^{-19}	13	[23]
	m	0.657	13	[23]
	τ_0	40	13	
Viscoplastic dashpot	a	0.1	18	
	$\ddot{b}$	$22\omega_w + 0.8$	18	
	σ_0(MPa)	$30X$	18	
Energy release rate	G_c^0 (N/mm)	190	43	[24]
Length scale parameter	l_0 (mm)	0.5	43	[24]
σ_d	σ_d (MPa)	$85X$	45	
Moisture swelling coefficient	a_w	0.039	4	[24]

it has some limitations when compared to the experimental data. The deviation from the experimental results could be attributed to the formulation of the constitutive model itself as well as the unique set of material parameters used. Nevertheless, the amplification approach employed in this study to account for the effects of moisture and BNP contents has resulted in realistic numerical predictions. Additionally, by calibrating the viscoplastic flow and modifying the crack driving force, we are able to reasonably predict the evolution of plasticity and damage in the nanocomposites. Figure 8 show contour plots of the phase-field variable for the BNP (5 wt%)/epoxy specimen at different load steps of the simulations corresponding to the imposed displacements of 3.18, 3.21, 3.22, and 3.25 mm. The snapshots are taken at the points indicated in Fig. 7a.

Next, dogbone tensile tests are conducted to evaluate the capability of the PFM model in predicting the fracture behavior of BNP/epoxy nanocomposites with 10 wt% of BNPs. The simulations are performed using the calibrated material parameters listed in Table 3, and the effect of nanoparticle contents is taken into account using the amplification factor presented in Eq. (30). Figure 9a, b show the effect of BNP weight fraction on the force–displacement response at the deformation rate of $\dot{u} = 1$ mm/min and $\theta = 296$ K. Both experimental data and numerical predictions are presented in the figures. In these curves, good agreements are observed between the numerical results and experimental data, evidencing the practicability of the PFM at different BNP weight fractions. Contour plots of the phase-field variable for the BNP (10 wt%)/epoxy specimen at imposed displacements of 3.17, 3.18, 3.19, and 3.20 mm are shown in Fig. 10. The plots correspond to the points indicated in Fig. 9a.

We then explore how temperature affect the fracture behavior of BNP/epoxy nanocomposites under cyclic loading. The results of dogbone simulation tests, presented in Fig. 11, show that specimens fractures at different displacement ranges depending on the temperature: around 3.0 mm at 253 K, around 4.2 mm at 296 K, and around 7.0 mm at 323 K. These observations can interpreted in two ways. First, as temperature increases, the shear and bulk modulus associated with the equilibrium, non-equilibrium, and volumetric responses decrease (see Eqs. 31 and 32), resulting in a less stiff material. Second, the deformation of the viscoelastic composite is temperature-dependent, meaning that an increase in temperature leads to a greater displacement at the fracture initiation due to a rise in the viscous flow. Figures 12, 13, 14 show the crack phase-field and von Mises equivalent plastic strain field at the incipient and final stage of cracking at 253, 296, and 323 K. The plastic strain is calculated by $\bar{\mathbf{E}}_{vp} = \frac{1}{2}\left(\bar{\mathbf{F}}_{vp}^{T}\bar{\mathbf{F}}_{vp} - \mathbf{I}\right)$. According to the figures, the cracks firstly appear at the location of the plastic stress concentration at the notches. The initial cracks propagate within the plastic strain localization band, leading to complete failure in the middle of the specimen. The figures also show that plastic deformation increases by increasing temperature.

The fracture behavior of BNP/epoxy nanocomposites under cyclic and monolithic loading is analyzed in Figs. 15, 16, 17. The results of dogbone simulation tests present the force–displacement behavior of saturated BNP (10 wt%)/epoxy samples at three different temperatures—253, 296, and 323 K. The simulation results show that the displacement at fracture decreased from 3.0 to 2.3 mm at 253 K, from 4.2 to 3.5 mm at 296 K, and from 7.3 to 7.0 mm at 323 K, respectively. The results demonstrate that the magnitude of the recoverable and permanent strain strongly depends on thermomechanical cycles particularly at lower temperatures. The complex behavior of epoxy nanocomposites, where cyclic loading affects stress relaxation, viscoelastic strain

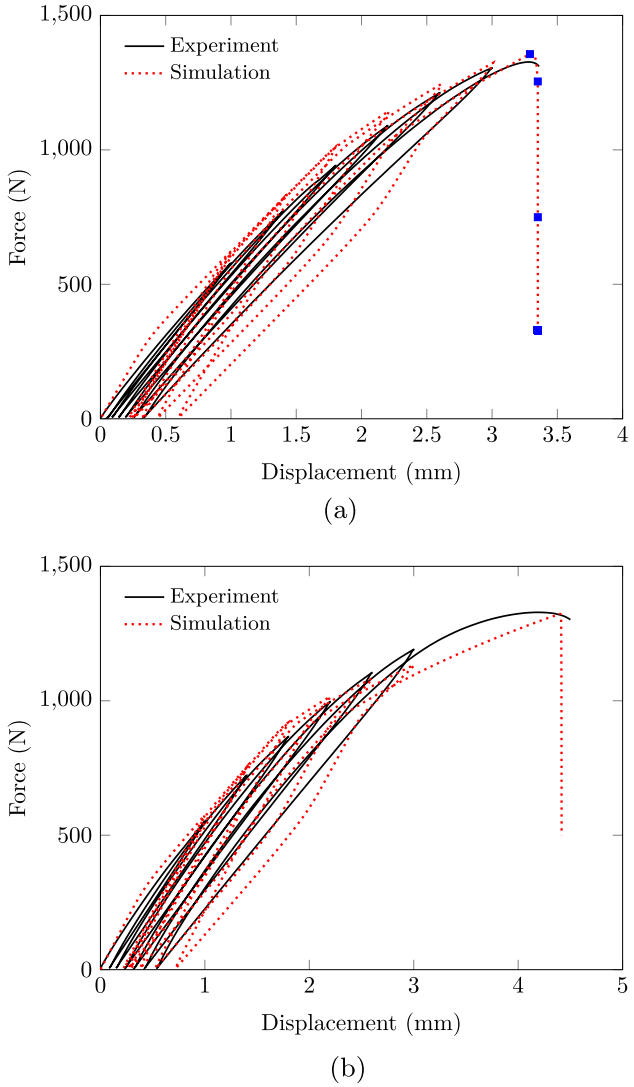

Fig. 4 Effect of moisture on the force–displacement response of the epoxy at room temperature and the deformation rate of 1 mm/min: **a** dry sample, and **b** saturated sample

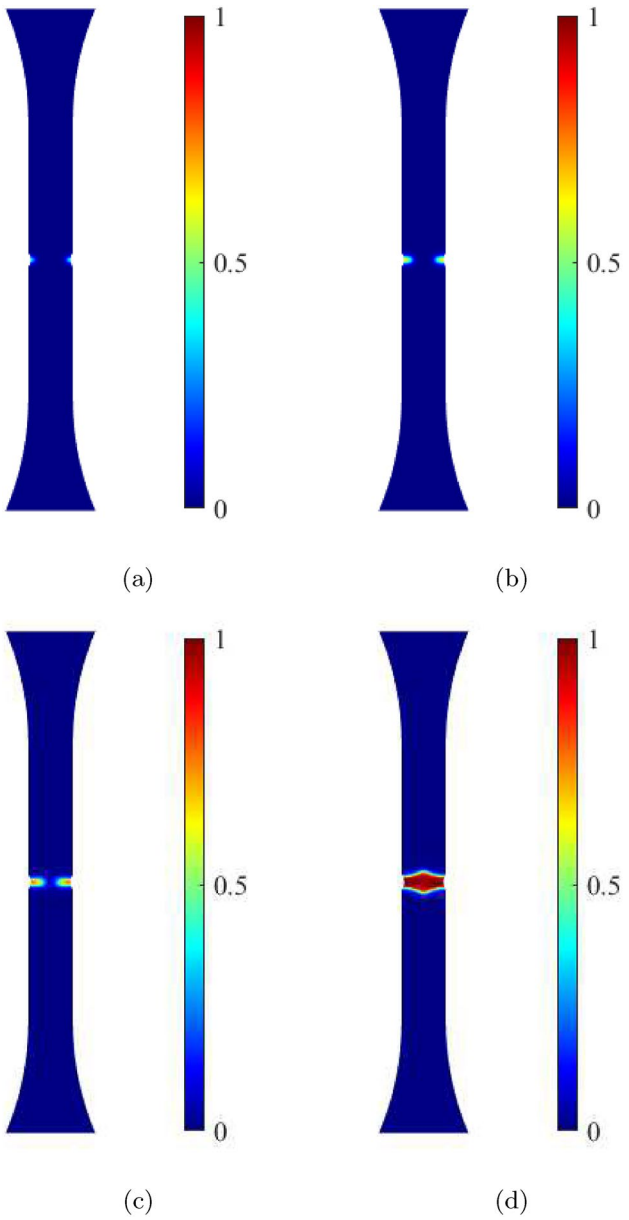

Fig. 5 Contour plots of the phase-field variable for the dry epoxy specimen at imposed displacements of **a** 3.29 mm, **b** 3.34 mm, **c** 3.35 mm, and **d** 3.3504 mm. Snapshots are taken at the points indicated in Fig. 4a

recovery, and permanent plastic strain, leads to different fracture behavior. It is important to note that the simulations assume the effect of temperature on the energy release rate to be negligible. While this assumption is acceptable based on experimental observations, further numerical–experimental validations are recommended to identify the variation of energy release rate with temperature accurately.

The growth of two edge cracks in a square subjected to uniaxial tension shown in Fig. 18 is then studied. The tensile load is applied at a deformation rate of $\dot{u} = 1$ mm/min with constant displacement increments of 10^{-4} mm. The simulations are performed at 296 K under plane strain conditions using the material parameters in Table 3. Meshes are refined in areas where cracks are expected to propagate, and a discretization with 4066 elements and an effective element size of 0.1 mm is generated in the central strip of the specimen. Figure 19a–c present the evolution of the crack phase-field and von Mises equivalent plastic strain field at three loading stages. The force–displacement curves related to dry and saturated BNP (10 wt%)/epoxy samples are also shown in Fig. 20. In the present model, the amplification factor defined by Eq. (30) captures the effect of moisture content on the material behavior of the nanocomposites. The moisture content causes a decrease in the shear and bulk modulus associated with the

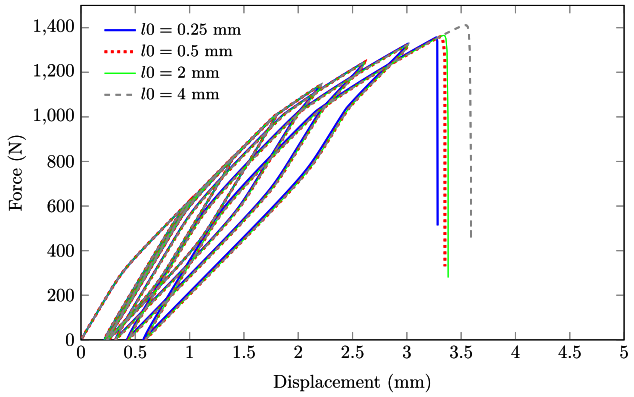

Fig. 6 Force–displacement response of the dry epoxy specimen for different length scale parameters

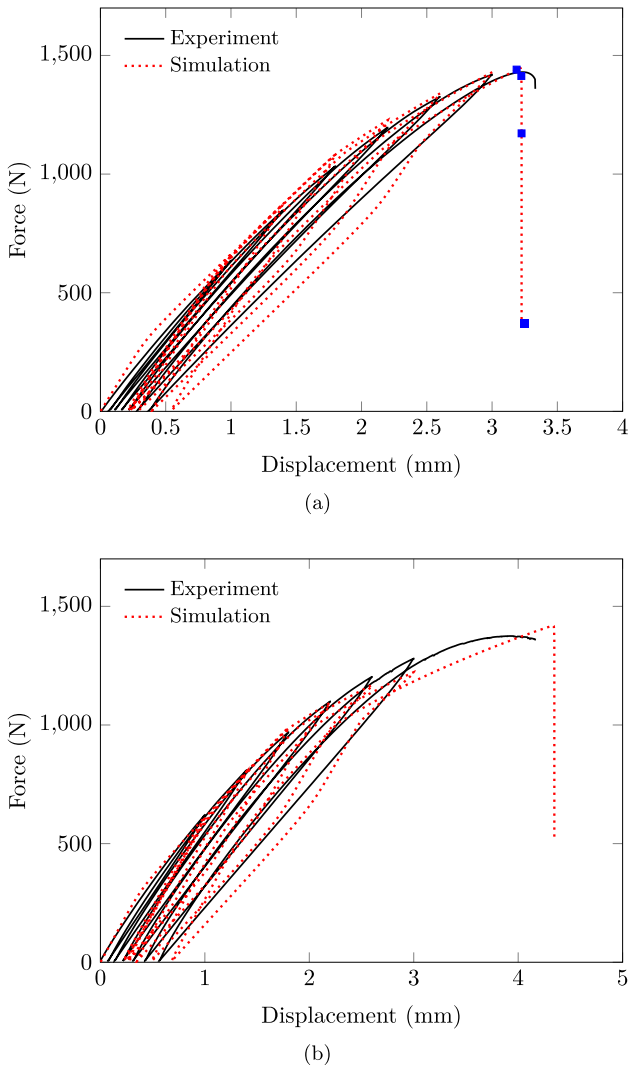

Fig. 7 Effect of moisture on the force–displacement response of BNP(5 wt%)/epoxy at room temperature and the deformation rate of 1 mm/min: **a** dry sample, and **b** saturated sample

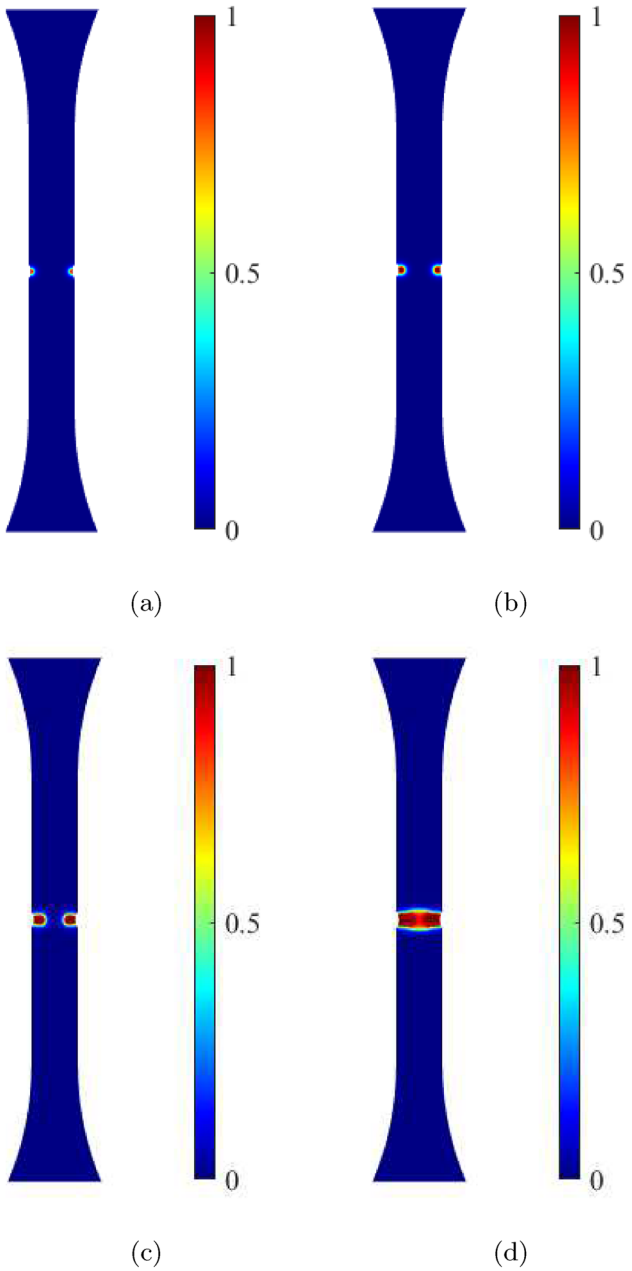

Fig. 8 Contour plots of the phase-field variable for the BNP(5 wt%)/epoxy specimen at imposed displacements of **a** 3.18 mm, **b** 3.21 mm, **c** 3.22 mm, and **d** 3.25 mm. Snapshots are taken at the points indicated in Fig. 7a

equilibrium, non-equilibrium, and volumetric responses, resulting in a less stiff material. Consequently, the saturated sample's peak force decreases from around 124 to 119 N. Furthermore, in contrast to the dogbone tensile simulations, a phenomenon observed in these simulations of the pre-cracked plates is that a stable crack propagates within the samples, resulting from the localization mainly occurring in front of the crack tip as can be seen in the contour plots in Fig. 19a–c.

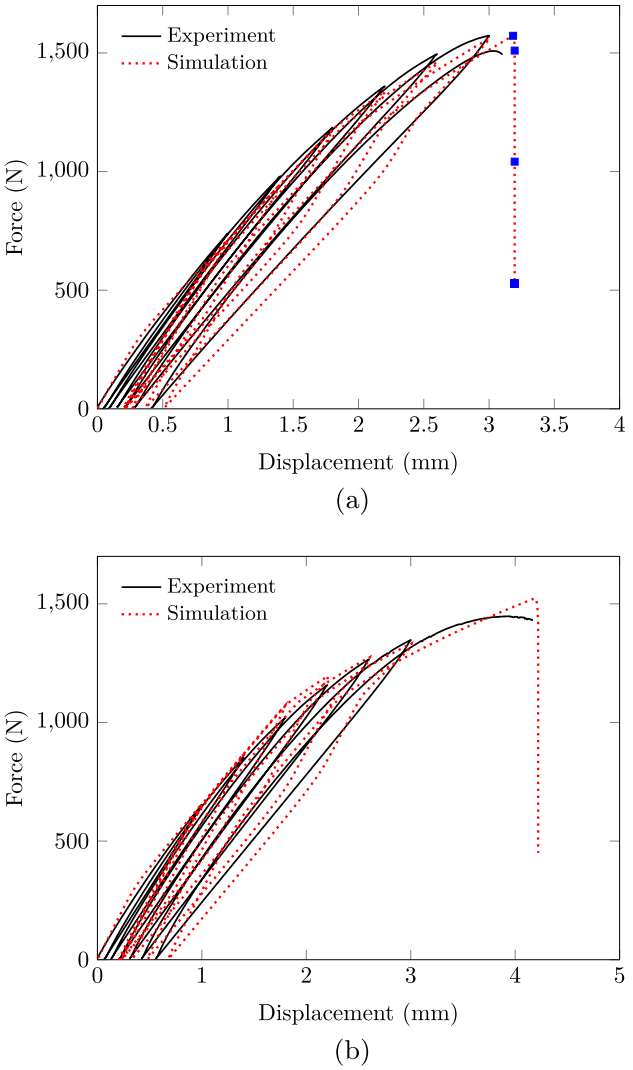

Fig. 9 Effect of moisture on the force–displacement response of BNP(10 wt%)/epoxy at room temperature and the deformation rate of 1 mm/min: **a** dry sample, and **b** saturated sample

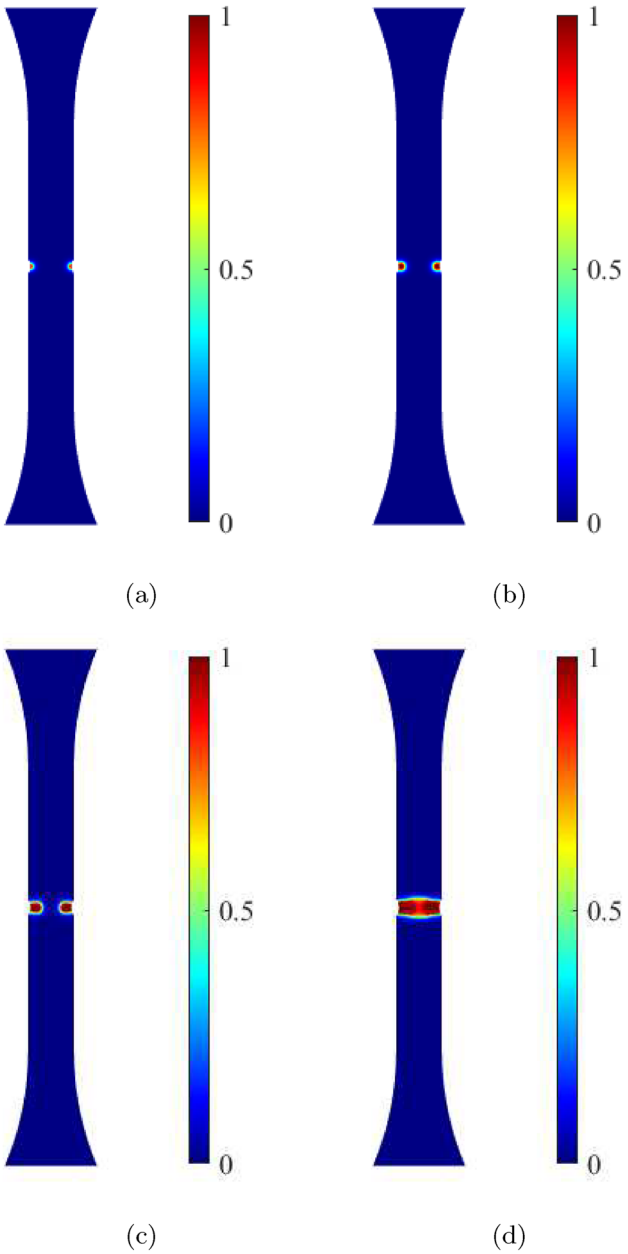

Fig. 10 Contour plots of the phase-field variable for the dry BNP(10 wt%)/epoxy specimen at imposed displacements of **a** 3.17 mm, **b** 3.18 mm, **c** 3.19 mm, and **d** 3.20 mm. Snapshots are taken at the points indicated in Fig. 9a

The proposed model's ability to predict fracture patterns is evaluated by conducting single-edge notched tensile and shear tests on pure epoxy samples. The geometry and boundary conditions of the tests are shown in Fig. 21. A horizontal notch is placed at the center of the specimen's left outer surface. The bottom side of the specimen is fixed, while the top side is moved. Both tensile and shear loads are applied at a deformation rate of $\dot{u} = 1$ mm/min with constant displacement increments of 10^{-6} mm. The simulations are performed at 296 K under plane strain conditions using the material parameters listed in Table 3, while the scale parameter is taken to be 0.015 mm. Meshes are refined in areas where cracks are expected to propagate.

For the tensile test, a discretization with 12,509 elements and an effective element size of 0.003 mm is generated in the central strip of the specimen. To reach the same element size at the critical zone in the shear test, 21,045 elements with refined meshes in the lower right diagonal strip of the specimen are used. The evolution of the crack phase-field and von Mises equivalent plastic strain field for the two samples under under unidirectional tension ($\alpha = 90°$) and pure shear deformation ($\alpha = 0°$) are respectively shown in Fig. 22a–c and 23a–c at three loading stages. It can be

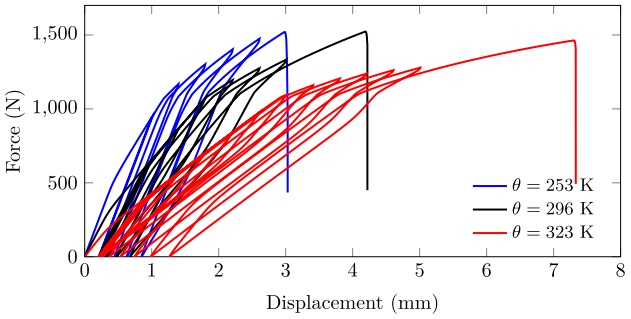

Fig. 11 Effect of temperature on the force–displacement response of the saturated BNP(10 wt%)/epoxy samples in dogbone simulation tests at the deformation rate of 1 mm/min

observed that the crack path is horizontal for the tensile case, while there is a curved crack path for the pure shear case. From the shear test in Figs. 23a–c, it can be found that the fracture mechanics-based crack driving force presented in Eq. (46) prevents cracking in compression. The crack patterns obtained are consistent with those reported in the literature [43]. The force–displacement curves for saturated BNP(10 wt%)/epoxy samples under tensile and shear load at a deformation rate of 1 mm/min and room temperature are shown in Fig. 24.

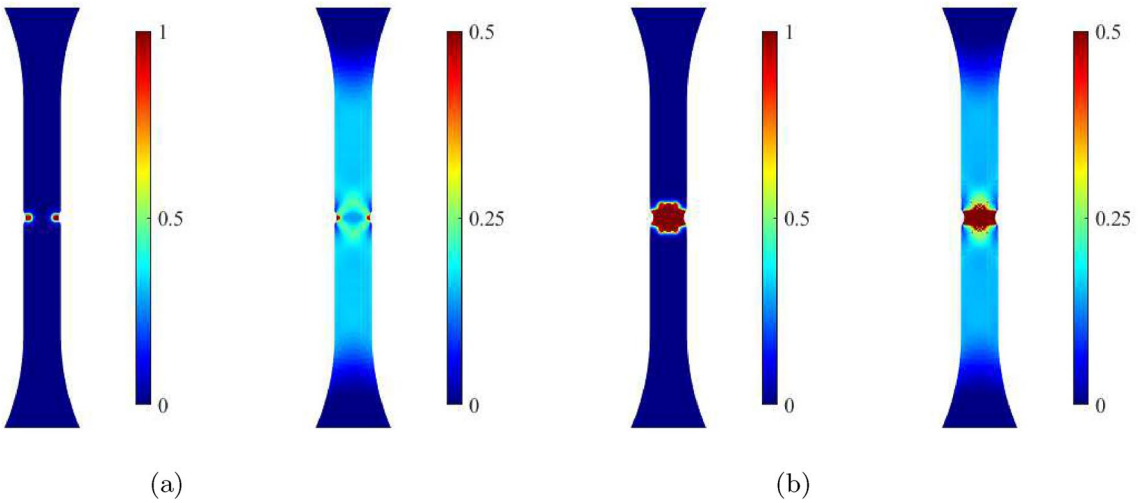

Fig. 12 Contour plots of damage (right) and equivalent plastic strain (left) in the saturated BNP(10 wt%)/epoxy samples under cyclic loading for imposed displacements of **a** 3.01 mm, and **b** 3.02 mm. The deformation rate is 1 mm/min, and temperature is 253 K

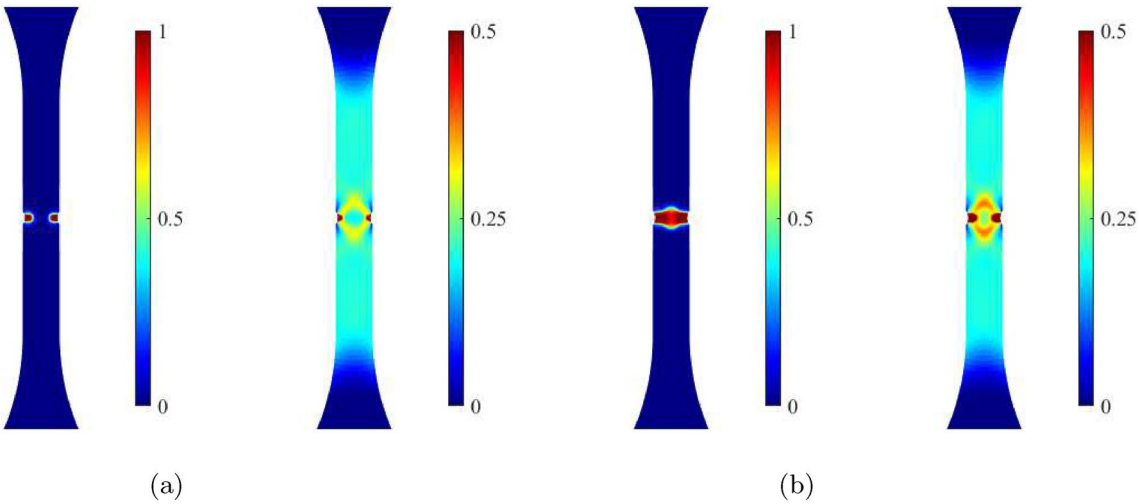

Fig. 13 Contour plots of damage (right) and equivalent plastic strain (left) in the saturated BNP(10 wt%)/epoxy samples under cyclic loading for imposed displacements of **a** 4.21 mm, and **b** 4.22 mm. The deformation rate is 1 mm/min, and temperature is 296 K

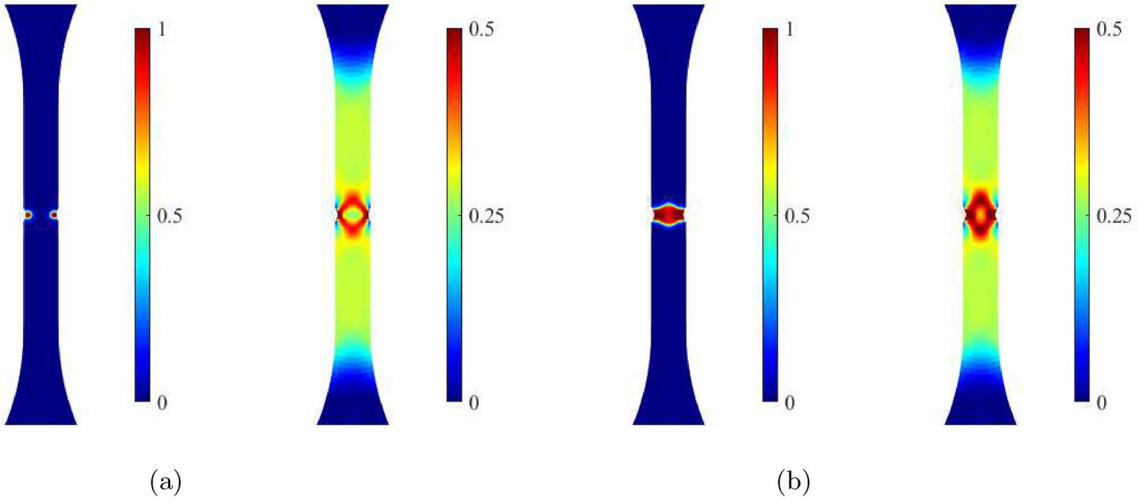

Fig. 14 Contour plots of damage (right) and equivalent plastic strain (left) in the saturated BNP(10 wt%)/epoxy samples under cyclic loading for imposed displacements of **a** 7.06 mm, and **b** 7.07 mm. The deformation rate is 1 mm/min, and temperature is 323 K

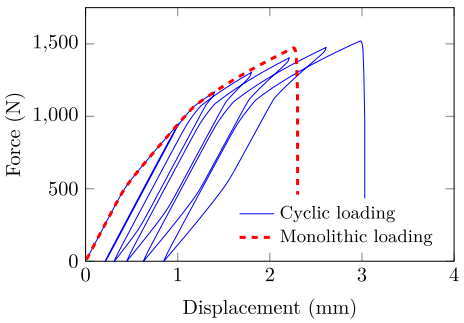

Fig. 15 Force–displacement response of saturated BNP(10 wt%)/epoxy samples in dogbone simulation tests under cyclic and monolithic loading at 253 K

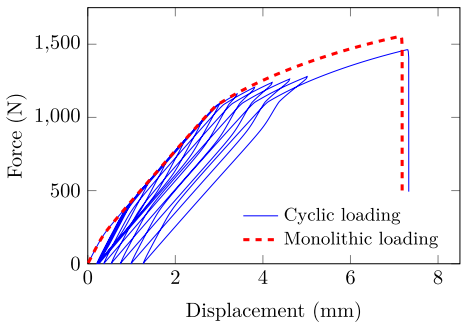

Fig. 17 Force–displacement response of saturated BNP(10 wt%)/epoxy samples in dogbone simulation tests under cyclic and monolithic loading at 323 K

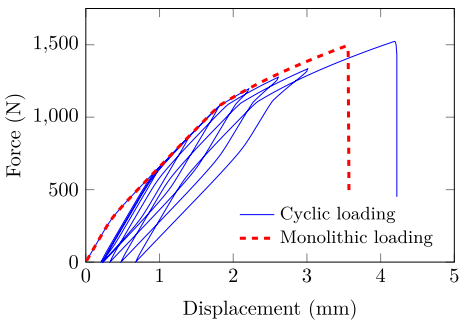

Fig. 16 Force–displacement response of saturated BNP(10 wt%)/epoxy samples in dogbone simulation tests under cyclic and monolithic loading at 296 K

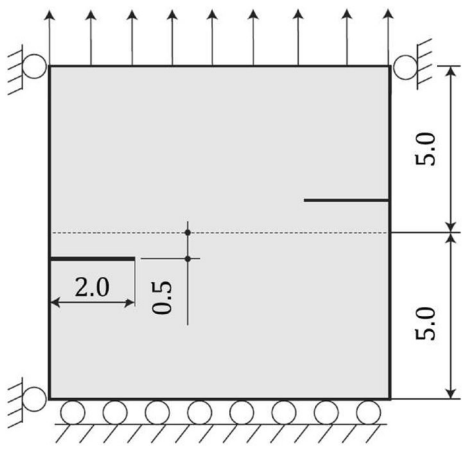

Fig. 18 Geometry and boundary conditions of a square plate with two edge cracks under uniaxial tension

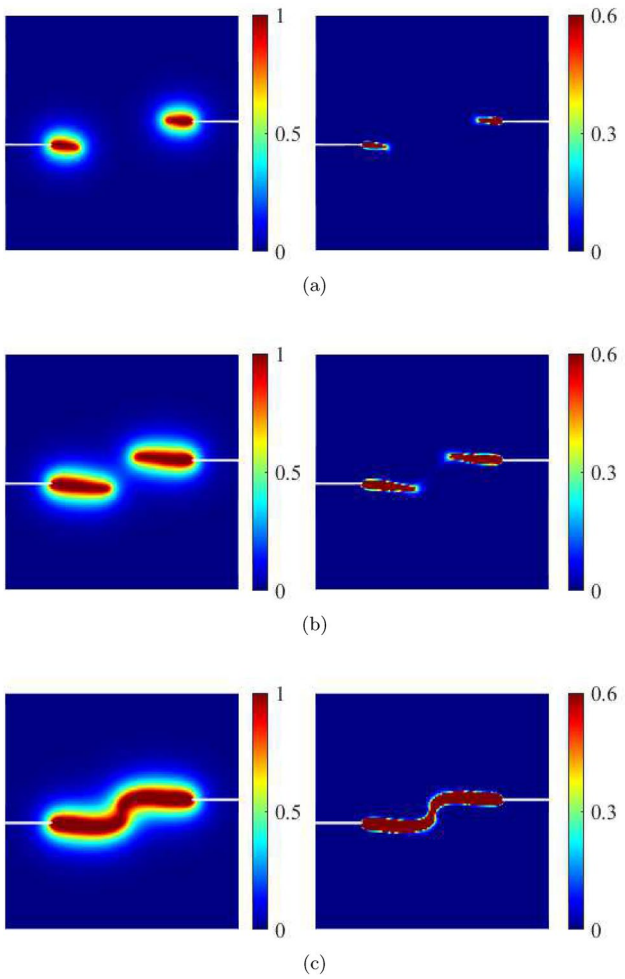

Fig. 19 Contour plots of damage (right) and equivalent plastic strain (left) in a saturated BNP(10 wt%)/epoxy sample under monolithic loading at the deformation rate of 1 mm/min for imposed displacements of **a** 0.035 mm, **b** 0.040 mm, and **c** 0.045 mm

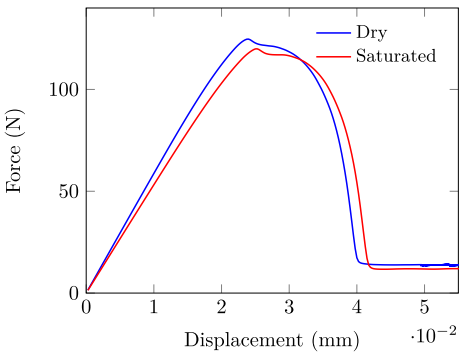

Fig. 20 Force–displacement curve of saturated BNP(10 wt%)/epoxy at room temperature the deformation rate of 1 mm/min

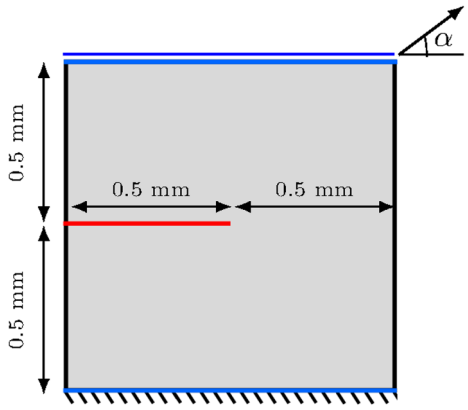

Fig. 21 Geometry and boundary conditions of single edge notched specimens

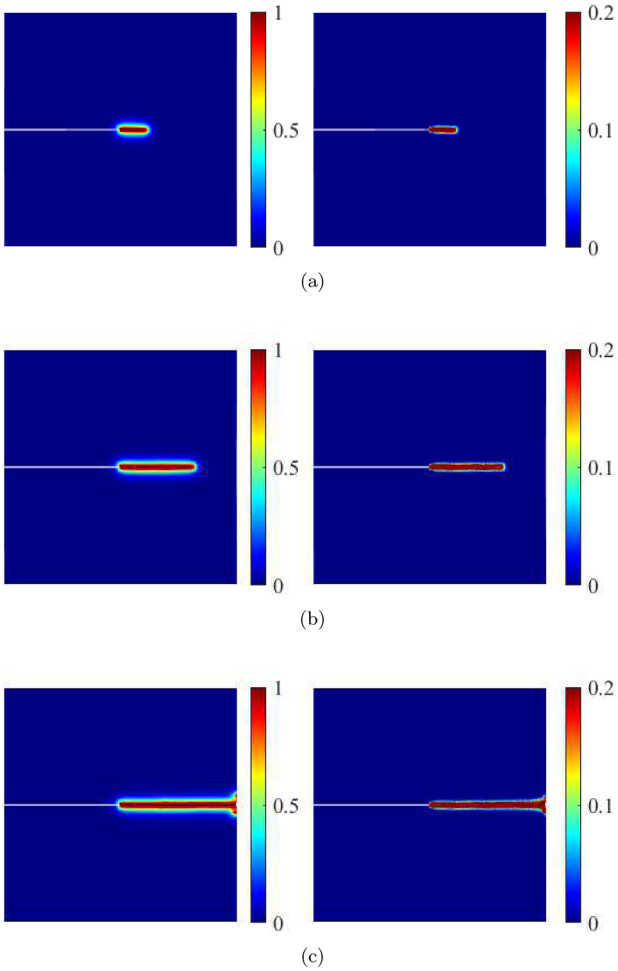

Fig. 22 Contour plots of damage (right) and equivalent plastic strain (left) in the saturated BNP(10 wt%)/epoxy samples under unidirectional tension ($\alpha = 90°$) at the deformation rate of 1 mm/min and imposed displacements of **a** 0.0027 mm, **b** 0.0029 mm, and **c** 0.0031 mm

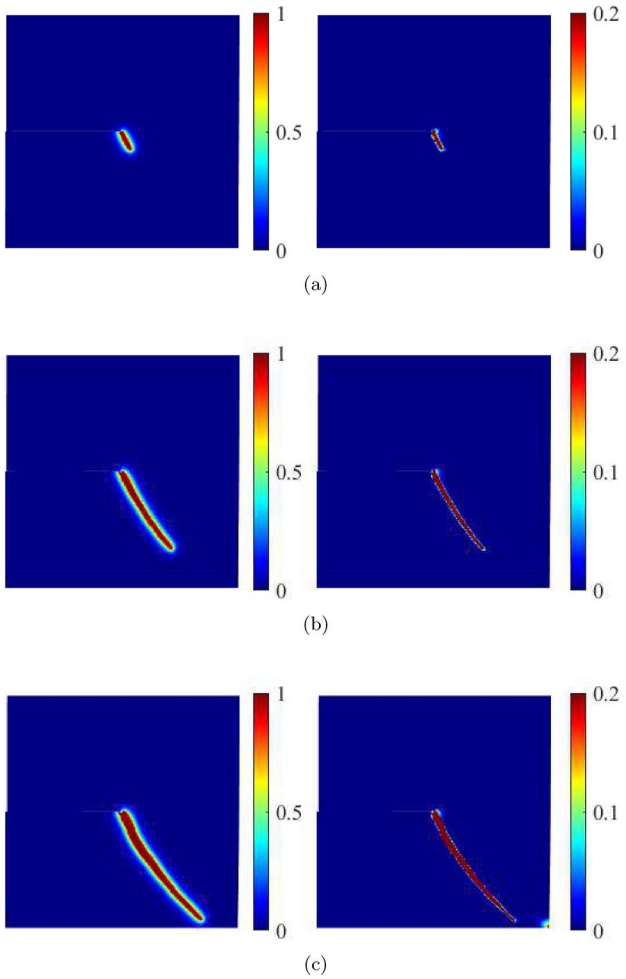

Fig. 23 Contour plots of damage (right) and equivalent plastic strain (left) in the saturated BNP(10 wt%)/epoxy samples under pure shear deformation ($\alpha = 0°$) at the deformation rate of 1 mm/min and imposed displacements of **a** 0.0027 mm, **b** 0.0029 mm, and **c** 0.0031 mm

5 Summary and conclusions

A finite deformation phase-field fracture model has been developed to study the cyclic viscoelastic–viscoplastic fracture behavior of BNPs reinforced epoxy nanocomposites under hygrothermal conditions. For the realistic modeling of damage and viscoplasticity mechanisms in the nanocomposites, the PFM with a fracture mechanics-based crack driving force has been coupled to a viscoelastic–viscoplastic constitutive law. Within the derived formulation, a free energy has additively been decomposed into an equilibrium, a non-equilibrium, and a volumetric part, capturing the effect of nanoparticles, moisture and temperature on the nonlinear material behavior of the nanocomposites. Also, an amplification factora modified version of the Kitagawa model have been adopted to capture the role played by nanoparticles, moisture and temperature on the fracture behavior.

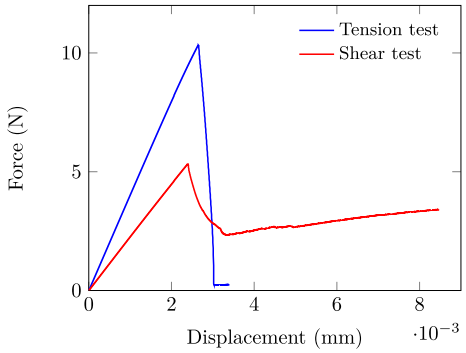

Fig. 24 Force–displacement curve of saturated BNP(10 wt%)/epoxy at room temperature the deformation rate of 1 mm/min

The proposed PFM has been implemented in the FE analysis of dogbone tensile tests to demonstrate its applicability. Numerical simulations were conducted to investigate the impact of nanoparticle content on the force–displacement response of dry and saturated BNP/epoxy samples subjected to cyclic loading–unloading. The results indicated that the force–displacement responses obtained from the numerical simulations were consistent with those of experimental tests at various nanoparticle and moisture contents. The comparison between numerical and experimental results confirms the capacity of the PFM in predicting the development of damage and viscoplasticity in BNP/epoxy nanocomposites at different nanoparticle and moisture contents.

To evaluate the proposed PFM's potential for broader applications, it would be worthwhile to compare the numerical predictions at different temperatures and deformation rates with experimental data in the future. Also, the physical and chemical interactions between nanoparticles and epoxy matrices undergo significant changes under finite deformation at the micro- and sub-micro-scale. These changes would impact other material properties, such as viscosity and energy release rate. However, due to the complex interactions at the interphase of nanoparticle/epoxy, the mechanisms leading to these changes are not clearly understood. In the proposed model, the changes are considered by taking the volume fraction of nanoparticles and moisture contents. To gain a deeper understanding of the microstructure's effect on the macroscopic properties, the PFM can be informed by molecular simulations [74, 75]. It would allow the analysis of the polymer nanocomposites at the molecular scale. Furthermore, an extension of the present phase-field formulations to account for the effect of non-isothermal conditions [76] on the fracture behavior of epoxy nanocomposites should be planned for the future studies.

Acknowledgements This work originates from two research projects: (1) "Challenges of industrial application of nanomodified and

hybrid material systems in lightweight rotor blade construction (HANNAH)", and (2) "Functionalized, multi-physically optimized adhesives for inherent structural health monitoring of rotor blades (Func2Ad)" funded by the Federal Ministry for Economic Affairs and Climate Action. The authors wish to express their gratitude for the financial support.

Author Contributions Behrouz Arash: Conceptualization, Investigation, Methodology, Coding, Writing-original draft, Writing-review and editing. Shadab Zakavati: Investigation, Methodology, Coding, Writing-review and editing. Betim Bahtiri: Investigation, Methodology, Coding, Writing-review and editing, Maximilian Jux: Investigation, Experiments, Writing-review and editing. Raimund Rolfes: Funding acquisition, Supervision, Writing-review and editing.

Funding Open access funding provided by OsloMet - Oslo Metropolitan University. The study was supported by the Federal Ministry of Economic Affairs and Climate Action (BMWK), grant number: FKZ 03EE3069 A-F.

Data availibility All data are available upon reasonable request.

Code availability All codes are available upon reasonable request.

Materials availability Not applicable.

Declarations

Conflict of interest The authors declare no conflict of interest or relationships that could influence the work.

Ethics approval and consent to participate Not applicable.

Consent for publication Not applicable.

References

1. Spitalsky Z, Tasis D, Papagelis K, Galiotis C (2010) Carbon nanotube-polymer composites: chemistry, processing, mechanical and electrical properties. Prog Polym Sci 35(3):357–401
2. Li Y, Wang S, Arash B, Wang Q (2016) A study on tribology of nitrile-butadiene rubber composites by incorporation of carbon nanotubes: molecular dynamics simulations. Carbon 100:145–150
3. Mousavi AA, Arash B, Rolfes R (2021) Optimization assisted coarse-grained modeling of agglomerated nanoparticle reinforced thermosetting polymers. Polymer 225:123741
4. Jux M, Fankhänel J, Daum B, Mahrholz T, Sinapius M, Rolfes R (2018) Mechanical properties of epoxy/boehmite nanocomposites in dependency of mass fraction and surface modification-an experimental and numerical approach. Polymer 141:34–45
5. Khorasani MGZ, Silbernagl D, Szymoniak P, Hodoroaba V-D, Sturm H (2019) The effect of boehmite nanoparticles (γ-alooh) on nanomechanical and thermomechanical properties correlated to crosslinking density of epoxy. Polymer 164:174–182
6. Arash B, Exner W, Rolfes R (2019) A viscoelastic damage model for nanoparticle/epoxy nanocomposites at finite strain: a multiscale approach. J Mech Phys Solids 128:162–180
7. Bardella L (2001) A phenomenological constitutive law for the nonlinear viscoelastic behaviour of epoxy resins in the glassy state. Eur J Mech A Solids 20(6):907–924
8. Zhou Y, Pervin F, Lewis L, Jeelani S (2007) Experimental study on the thermal and mechanical properties of multi-walled carbon nanotube-reinforced epoxy. Mater Sci Eng A 452:657–664
9. Vogler M, Rolfes R, Camanho P (2013) Modeling the inelastic deformation and fracture of polymer composites-part i: plasticity model. Mech Mater 59:50–64
10. Vu-Bac N, Bessa M, Rabczuk T, Liu WK (2015) A multiscale model for the quasi-static thermo-plastic behavior of highly crosslinked glassy polymers. Macromolecules 48(18):6713–6723
11. Nguyen V-D, Lani F, Pardoen T, Morelle X, Noels L (2016) A large strain hyperelastic viscoelastic-viscoplastic-damage constitutive model based on a multi-mechanism non-local damage continuum for amorphous glassy polymers. Int J Solids Struct 96:192–216
12. Park H, Choi J, Kim B, Yang S, Shin H, Cho M (2018) Toward the constitutive modeling of epoxy matrix: Temperature-accelerated quasi-static molecular simulations consistent with the experimental test. Composites B 142(1):131–141
13. Boyce M, Socrate S, Llana P (2000) Constitutive model for the finite deformation stress-strain behavior of poly (ethylene terephthalate) above the glass transition. Polymer 41(6):2183–2201
14. Qi H, Boyce M (2005) Stress-strain behavior of thermoplastic polyurethanes. Mech Mater 37(8):817–839
15. Li Y, Tang S, Kröger M, Liu WK (2016) Molecular simulation guided constitutive modeling on finite strain viscoelasticity of elastomers. J Mech Phys Solids 88:204–226
16. Nguyen T, Lejeunes S, Eyheramendy D, Boukamel A (2016) A thermodynamical framework for the thermo-chemo-mechanical couplings in soft materials at finite strain. Mech Mater 95:158–171
17. Fankhänel J, Arash B, Rolfes R (2019) Elastic interphase properties of nanoparticle/epoxy nanocomposites: a molecular dynamics study. Composites B Eng 176:107211
18. Arash B, Exner W, Rolfes R (2019) Viscoelastic damage behavior of fiber reinforced nanoparticle-filled epoxy nanocomposites: multiscale modeling and experimental validation. Composites B Eng 174:107005
19. Unger R, Exner W, Arash B, Rolfes R (2019) Non-linear viscoelasticity of epoxy resins: molecular simulation-based prediction and experimental validation. Polymer 180:121722
20. Unger R, Arash B, Exner W, Rolfes R (2020) Effect of temperature on the viscoelastic damage behaviour of nanoparticle/epoxy nanocomposites: constitutive modelling and experimental validation. Polymer 191:122265
21. Chowdhury K, Talreja R, Benzerga AA (2008) Effects of manufacturing-induced voids on local failure in polymer-based composites. J Eng Mater Technol 130(2):021010
22. Bahtiri B, Arash B, Rolfes R (2022) Elucidating atomistic mechanisms underlying water diffusion in amorphous polymers: an autonomous basin climbing-based simulation method. Comput Mater Sci 212:111565
23. Bahtiri B, Arash B, Scheffler S, Jux M, Rolfes R (2023) A machine learning-based viscoelastic-viscoplastic model for epoxy nanocomposites with moisture content. Comput Methods Appl Mech Eng 415:116293. https://doi.org/10.1016/j.cma.2023.116293

24. Arash B, Exner W, Rolfes R (2023) Effect of moisture on the nonlinear viscoelastic fracture behavior of polymer nanocompsites: a finite deformation phase-field model. Eng Comput 39(1):773–790
25. Mmari W, Johannesson B (2022) A model for multiphase moisture and heat transport below and above the saturation point of deformable and swelling wood fibers-ii: Hygro-mechanical response. Appl Eng Sci 12:100118
26. Needleman A (1988) Material rate dependence and mesh sensitivity in localization problems. Comput Methods Appl Mech Eng 67(1):69–85
27. Geers M, De Borst R, Brekelmans W, Peerlings R (1998) Strain-based transient-gradient damage model for failure analyses. Comput Methods Appl Mech Eng 160(1–2):133–153
28. Hillerborg A, Modéer M, Petersson P-E (1976) Analysis of crack formation and crack growth in concrete by means of fracture mechanics and finite elements. Cem Concr Res 6(6):773–781
29. Xu X-P, Needleman A (1994) Numerical simulations of fast crack growth in brittle solids. J Mech Phys Solids 42(9):1397–1434
30. Belytschko T, Fish J, Engelmann BE (1988) A finite element with embedded localization zones. Comput Methods Appl Mech Eng 70(1):59–89
31. Moës N, Dolbow J, Belytschko T (1999) A finite element method for crack growth without remeshing. Int J Numer Meth Eng 46(1):131–150
32. Wells GN, Sluys L (2001) A new method for modelling cohesive cracks using finite elements. Int J Numer Meth Eng 50(12):2667–2682
33. Belytschko T, Chen H, Xu J, Zi G (2003) Dynamic crack propagation based on loss of hyperbolicity and a new discontinuous enrichment. Int J Numer Meth Eng 58(12):1873–1905
34. Sukumar N, Dolbow J, Moës N (2015) Extended finite element method in computational fracture mechanics: a retrospective examination. Int J Fract 196:189–206
35. Peerlings RH, Borst R, Brekelmans WM, De Vree J (1996) Gradient enhanced damage for quasi-brittle materials. Int J Numer Meth Eng 39(19):3391–3403
36. Saroukhani S, Vafadari R, Simone A (2013) A simplified implementation of a gradient-enhanced damage model with transient length scale effects. Comput Mech 51(6):899–909
37. Poh LH, Sun G (2017) Localizing gradient damage model with decreasing interactions. Int J Numer Methods Eng 110(6):503–522
38. Vandoren B, Simone A (2018) Modeling and simulation of quasi-brittle failure with continuous anisotropic stress-based gradient-enhanced damage models. Comput Methods Appl Mech Eng 332:644–685
39. Arash B, Exner W, Rolfes R (2021) A finite deformation phase-field fracture model for the thermo-viscoelastic analysis of polymer nanocomposites. Comput Methods Appl Mech Eng 381:113821
40. Francfort GA, Marigo J-J (1998) Revisiting brittle fracture as an energy minimization problem. J Mech Phys Solids 46(8):1319–1342
41. Aranson I, Kalatsky V, Vinokur V (2000) Continuum field description of crack propagation. Phys Rev Lett 85(1):118
42. Miehe C, Welschinger F, Hofacker M (2010) Thermodynamically consistent phase-field models of fracture: variational principles and multi-field fe implementations. Int J Numer Meth Eng 83(10):1273–1311
43. Miehe C, Hofacker M, Welschinger F (2010) A phase field model for rate-independent crack propagation: robust algorithmic implementation based on operator splits. Comput Methods Appl Mech Eng 199(45–48):2765–2778
44. Bourdin B, Francfort GA, Marigo J-J (2000) Numerical experiments in revisited brittle fracture. J Mech Phys Solids 48(4):797–826
45. Wu J-Y (2017) A unified phase-field theory for the mechanics of damage and quasi-brittle failure. J Mech Phys Solids 103:72–99
46. Ambati M, Kruse R, De Lorenzis L (2016) A phase-field model for ductile fracture at finite strains and its experimental verification. Comput Mech 57(1):149–167
47. Miehe C, Mauthe S (2016) Phase field modeling of fracture in multi-physics problems. Part iii. crack driving forces in hydro-poro-elasticity and hydraulic fracturing of fluid-saturated porous media. Comput Methods Appl Mech Eng 304:619–655
48. Dammaß F, Kalina KA, Ambati M, Kästner M (2023) Phase-field modelling and analysis of rate-dependent fracture phenomena at finite deformation. Comput Mech 72:859–883
49. Cui C, Ma R, Martínez-Pañeda E (2023) Electro-chemo-mechanical phase field modeling of localized corrosion: theory and comsol implementation. Eng Comput 39(6):3877–3894
50. Au-Yeung K, Quintanas-Corominas A, Martínez-Pañeda E, Tan W (2023) Hygroscopic phase field fracture modelling of composite materials. Eng Comput 39(6):3847–3864
51. Greco L, Patton A, Negri M, Marengo A, Perego U, Reali A (2024) Higher order phase-field modeling of brittle fracture via isogeometric analysis. Eng Comput. https://doi.org/10.1007/s00366-024-01949-5
52. Shanthraj P, Sharma L, Svendsen B, Roters F, Raabe D (2016) A phase field model for damage in elasto-viscoplastic materials. Comput Methods Appl Mech Eng 312:167–185
53. Dean A, Kumar PAV, Reinoso J, Gerendt C, Paggi M, Mahdi E, Rolfes R (2020) A multi phase-field fracture model for long fiber reinforced composites based on the puck theory of failure. Composite Struct 251:112446
54. Msekh MA, Silani M, Jamshidian M, Areias P, Zhuang X, Zi G, He P, Rabczuk T (2016) Predictions of j integral and tensile strength of clay/epoxy nanocomposites material using phase field model. Composites B Eng 93:97–114
55. Goswami S, Anitescu C, Chakraborty S, Rabczuk T (2020) Transfer learning enhanced physics informed neural network for phase-field modeling of fracture. Theoret Appl Fract Mech 106:102447
56. Goswami S, Anitescu C, Rabczuk T (2020) Adaptive fourth-order phase field analysis using deep energy minimization. Theoret Appl Fract Mech 107:102527
57. Shen R, Waisman H, Guo L (2019) Fracture of viscoelastic solids modeled with a modified phase field method. Comput Methods Appl Mech Eng 346:862–890
58. Loew PJ, Peters B, Beex LA (2019) Rate-dependent phase-field damage modeling of rubber and its experimental parameter identification. J Mech Phys Solids 127:266–294
59. Yin B, Kaliske M (2020) Fracture simulation of viscoelastic polymers by the phase-field method. Comput Mech 65(2):293–309
60. Brighenti R, Rabczuk T, Zhuang X (2021) Phase field approach for simulating failure of viscoelastic elastomers. Eur J Mech A Solids 85:104092
61. Govindjee S, Reese S (1997) A presentation and comparison of two large deformation viscoelasticity models. J Eng Mater Technol 119(3):251–255
62. Boyce MC, Parks DM, Argon AS (1988) Large inelastic deformation of glassy polymers. Part i: rate dependent constitutive model. Mech Mater 7(1):15–33
63. Poulain X, Benzerga A, Goldberg R (2014) Finite-strain elasto-viscoplastic behavior of an epoxy resin: experiments and modeling in the glassy regime. Int J Plast 62:138–161
64. Bergström J, Hilbert L Jr (2005) A constitutive model for predicting the large deformation thermomechanical behavior of fluoropolymers. Mech Mater 37(8):899–913
65. Guth E (1945) Theory of filler reinforcement. J Appl Phys 16(1):20–25

66. Wu J-Y, Nguyen VP, Nguyen CT, Sutula D, Sinaie S, Bordas SP (2020) Phase-field modeling of fracture. Adv Appl Mech 53:1–183
67. Bilgen C, Weinberg K (2019) On the crack-driving force of phase-field models in linearized and finite elasticity. Comput Methods Appl Mech Eng 353:348–372
68. Molnár G, Gravouil A (2017) 2d and 3d abaqus implementation of a robust staggered phase-field solution for modeling brittle fracture. Finite Elem Anal Des 130:27–38
69. Dean A, Reinoso J, Jha N, Mahdi E, Rolfes R (2020) A phase field approach for ductile fracture of short fibre reinforced composites. Theoret Appl Fract Mech 106:102495
70. Sun W, Chaikof EL, Levenston ME (2008) Numerical approximation of tangent moduli for finite element implementations of nonlinear hyperelastic material models. J Biomech Eng 130(6):061003
71. Miehe C (1996) Numerical computation of algorithmic (consistent) tangent moduli in large-strain computational inelasticity. Comput Methods Appl Mech Eng 134(3–4):223–240
72. Tomas I, Cisilino A, Frontini P (2008) Accurate, efficient and robust explicit and implicit integration schemes for the Arruda-Boyce viscoplastic model. Asociacion Argentina de Mecanica Computacional, Argentina
73. Ostwald R, Kuhl E, Menzel A (2019) On the implementation of finite deformation gradient-enhanced damage models. Comput Mech 64(3):847–877
74. Arash B, Park HS, Rabczuk T (2015) Tensile fracture behavior of short carbon nanotube reinforced polymer composites: a coarse-grained model. Compos Struct 134:981–988
75. Arash B, Park HS, Rabczuk T (2016) Coarse-grained model of the j-integral of carbon nanotube reinforced polymer composites. Carbon 96:1084–1092
76. Dittmann M, Aldakheel F, Schulte J, Schmidt F, Krüger M, Wriggers P, Hesch C (2020) Phase-field modeling of porous-ductile fracture in non-linear thermo-elasto-plastic solids. Comput Methods Appl Mech Eng 361:112730